Eddy-Induced Modulation of Turbulent Dissipation over Rough Topography in the Southern Ocean

J. ALEXANDER BREARLEY, KATY L. SHEEN, AND ALBERTO C. NAVEIRA GARABATO

Ocean and Earth Science, National Oceanography Centre Southampton, University of Southampton, Southampton, United Kingdom

DAVID A. SMEED

Marine Physics and Ocean Climate, National Oceanography Centre Southampton, Southampton, United Kingdom

STEPHANIE WATERMAN

Ocean and Earth Science, National Oceanography Centre Southampton, University of Southampton, Southampton, United Kingdom, and Climate Change Research Centre and ARC Centre of Excellence for Climate System Science, University of New South Wales, Sydney, New South Wales, Australia

(Manuscript received 6 November 2012, in final form 11 July 2013)

ABSTRACT

Mesoscale eddies are universal features of the ocean circulation, yet the processes by which their energy is dissipated remain poorly understood. One hypothesis argues that the interaction of strong geostrophic flows with rough bottom topography effects an energy transfer between eddies and internal waves, with the breaking of these waves causing locally elevated dissipation focused near the sea floor. This study uses hydrographic and velocity data from a 1-yr mooring cluster deployment in the Southern Ocean to test this hypothesis. The moorings were located over a small (~10 km) topographic obstacle to the east of Drake Passage in a region of high eddy kinetic energy, and one was equipped with an ADCP at 2800-m depth from which internal wave shear variance and dissipation rates were calculated. Examination of the ADCP time series revealed a predominance of upward-propagating internal wave energy and a significant correlation ($r = 0.45$) between shear variance levels and subinertial near-bottom current speeds. Periods of strong near-bottom flow coincided with increased convergence of eddy-induced interfacial form stress in the bottom 1500 m. Predictions of internal wave energy radiation were made from theory using measured near-bottom current speeds, and the mean value of wave radiation (5.3 mW m^{-2}) was sufficient to support the dissipated power calculated from the ADCP. A significant temporal correlation was also observed between radiated and dissipated power. Given the ubiquity of strong eddy flows and rough topography in the Southern Ocean, the transfer from eddy to internal wave energy is likely to be an important term in closing the ocean energy budget.

1. Introduction

In situ and satellite altimetric observations have shown that the ocean kinetic energy (KE) field in mid-to-high latitudes is dominated by mesoscale eddies on scales of 50–100 km. Maps of eddy kinetic energy (EKE; e.g., Wunsch and Stammer 1998), reveal an intensification of EKE in regions of large mean flows such as the Antarctic Circumpolar Current (ACC) as a result of baroclinic instability (Smith 2007), with a particular enhancement of EKE in frontal zones and immediately downstream of Drake Passage (Gille 1994; Morrow et al. 1994). The strength of this Southern Ocean eddy field is believed to be sensitive to climatic changes in forcing on a range of time scales (Thompson and Solomon 2002; Meredith and Hogg 2006; Meredith et al. 2012).

While the upscale transfer of eddy energy from high- to low-baroclinic modes (and ultimately to the barotropic mode) is relatively well quantified (Scott and Wang 2005), the processes by which eddy energy is dissipated are little understood. Ferrari and Wunsch (2009) review several candidate mechanisms including frictional

Corresponding author address: J. Alexander Brearley, Ocean and Earth Science, National Oceanography Centre Southampton, University of Southampton Waterfront Campus, European Way, Southampton, SO14 3ZH, United Kingdom.
E-mail: jab5@noc.soton.ac.uk

DOI: 10.1175/JPO-D-12-0222.1

bottom drag, loss of balance in the ocean interior, interactions with the internal wave field, continental margin absorption, and suppression by wind work. While friction in the bottom boundary layer is important, Wunsch and Ferrari (2004) argued that it is too weak to be the dominant sink. In addition, Molemaker et al. (2010) suggest that loss of balance is unlikely to be a large term in the deep ocean.

Another mechanism that has gained attention recently is the generation of gravity waves by geostrophic eddy flows impinging on small-scale (1–100 km) sea floor topography. The ACC contains several equivalent barotropic jets, such as those associated with the Polar Front (PF) and Subantarctic Front (SAF), and is therefore likely to be a zone of concentrated internal wave generation. Observations of near-bottom velocities in Drake Passage (Chereskin et al. 2009) have confirmed that large mesoscale velocities (occasionally exceeding $70\,\mathrm{cm\,s^{-1}}$) are present between the SAF and the PF. This is in contrast to other less-energetic regions, such as the Mid-Atlantic Ridge, where the generation mechanism for these gravity waves is believed to be barotropic tides (Polzin et al. 1997).

Whatever their generation mechanism, these gravity waves are thought to take the form of lee waves, which are phase locked to the topography and generally break within ~1 km of the sea floor, causing enhanced turbulent kinetic energy (TKE) dissipation. The theory of lee waves, initially developed by Bell (1975), has recently been generalized from two- to one-dimensional topography and modified to account for saturation of the energy radiation flux at steep topography (Nikurashin and Ferrari 2010a). Coarse-scale regional and global estimates of lee-wave energy radiation (Nikurashin and Ferrari 2010b; Scott et al. 2011) are now available.

Alongside the development of modified linear lee-wave theory, several Southern Ocean observational programs have found dissipation to be strongest in regions of rough topography, such as the western Drake Passage (Naveira Garabato et al. 2004) or around the Kerguelen Plateau (Waterman et al. 2013a). This signal has been observed by tracer measurements, which yield a time-integrated measure of diffusivity (Ledwell et al. 2011; Watson et al. 2013, manuscript submitted to *Nature*) and by spot measurements made using microstructure instruments, which infer mixing directly from centimeter-scale shear (St. Laurent et al. 2012; Sheen et al. 2013).

However, in the absence of long time series, it is difficult to quantify how eddy energy, extracted ultimately from wind work, is dissipated by molecular viscosity at centimeter scales. In addition, testing the applicability of lee-wave theory requires concurrent measurements of both TKE dissipation and near-bottom geostrophic flow speeds. Some indications that a transfer of energy between the eddy field and dissipative flow may be occurring can be surmised from recent literature. A 1-yr study on the East Pacific Rise (Liang and Thurnherr 2012) noted a strong correlation between subinertial flow and finescale–derived turbulent diffusivity, suggesting significant energy transfer between these scales. Furthermore, Nikurashin and Ferrari (2011) identified the East Pacific Rise as having elevated internal wave energy radiation. A 1-yr deployment of an Acoustic Doppler Current Profiler (ADCP) in Shag Rocks Passage suggested that turbulent mixing was modulated at subinertial time scales, with both 3.8 and 2.6 days being identified as important periods at which topographically trapped waves propagated from a local seamount (Damerell et al. 2011). However, details of the processes linking winds, eddies, tides, internal waves, and dissipation remain highly speculative.

In this study, we analyze hydrographic and velocity measurements collected by a cluster of moorings deployed for 1 yr to the east of Drake Passage and provide evidence for an energy transfer between the mesoscale eddy field and the internal wave motions that precede turbulent dissipation. The paper is structured as follows. In section 2, we discuss the mooring array location, the instrumentation used, and the sampling strategy employed. An overview of the hydrography is given in section 3a, with a focus on the movement of the SAF. Results of a time series of near bottom–integrated shear variance derived from an ADCP are discussed in section 3b, with attention directed toward the polarization of the internal wave energy and its frequency content. The significant correlation between shear variance levels and subinertial current speeds is discussed in section 3c, while the relationship between mesoscale velocities and internal wave kinetic energy is outlined in section 3d. The potential for tidal modulation of shear variance is examined in section 3e. In the discussion, it is proposed that deep eddy flows are accelerated at certain times by a convergence of the eddy-induced interfacial form stress in the bottom layers (section 4a). In section 4b, a quantitative comparison between the dissipated internal wave energy measured by the ADCP and lee-wave radiation from theory is made. Conclusions are outlined in section 5.

2. Data and methods

Data were collected as part of the Diapycnal and Isopycnal Mixing Experiment in the Southern Ocean (DIMES), a project tasked with quantifying and understanding the dissipation and physical controls of mixing in the Southern Ocean.

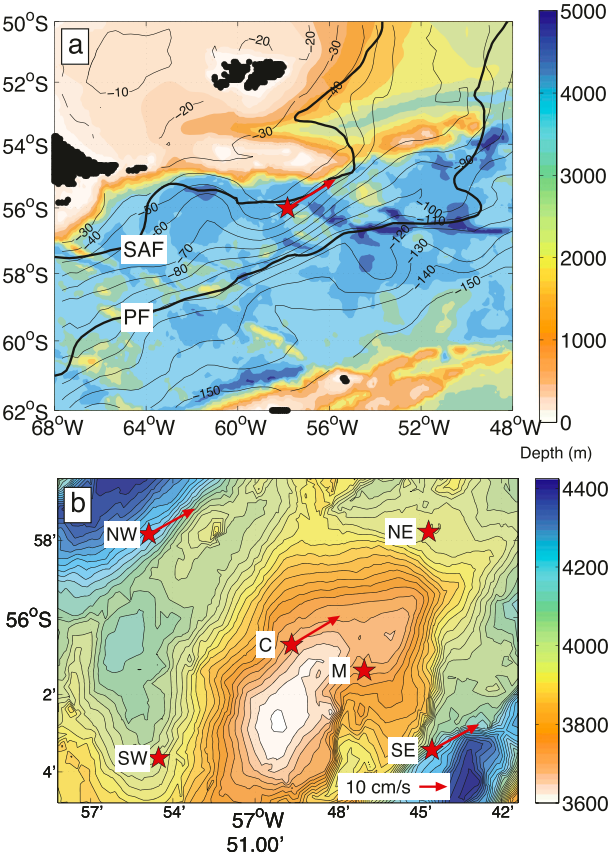

FIG. 1. (a) Location of DIMES mooring array (red star) with the direction of the mean current vector from the uppermost current meter (with an annual mean depth of 453 dbar) on the C mooring. Ocean bathymetry from the 5′ TerrainBase database is contoured in color (m), while black contours denote the mean sea surface height (SSH; m) for 12 Dec 2009–5 Dec 2010 derived from the 1/3° SSH anomaly of Archiving, Validation and Interpretation of Satellite Oceanographic data (AVISO) and the mean SSH of Maximenko et al. (2009). Climatological positions of the SAF and PF (Orsi et al. 1995) are marked. (b) Configuration of the mooring array, with mean annual current vectors close to 450 dbar shown for three of the moorings. Gridded multibeam bathymetry data collected in December 2010 are contoured. The TerrainBase dataset was created by the National Geophysical Data Center and World Data Center-A for Solid Earth Geophysics in Boulder, Colorado.

TABLE 1. List of instruments on the C mooring, located at 56°0.709′S, 57°49.661′W, for 12 Dec 2009–5 Dec 2010. In the first column, SMP stands for "serial interface, memory, and integral pump."

Instrument Type	Serial Number	Nominal depth (m)
Nortek acoustic current meter	6178	425
Seabird SMP MicroCAT	7304	425
Nortek acoustic current meter	6181	475
Seabird SMP MicroCAT	7305	475
Nortek acoustic current meter	6182	525
Seabird SMP MicroCAT	7306	525
Nortek acoustic current meter	6203	575
Seabird SMP MicroCAT	7307	575
Nortek acoustic current meter	6212	1201
Seabird SMP MicroCAT	7309	1201
Nortek acoustic current meter	6213	1299
Seabird SMP MicroCAT	7310	1299
Nortek acoustic current meter	6224	1853
Seabird SMP MicroCAT	7311	1853
Nortek acoustic current meter	6225	1951
Seabird SMP MicroCAT	7312	1951
Nortek acoustic current meter	6242	2049
Seabird SMP MicroCAT	7313	2049
Nortek acoustic current meter	6273	2152
Seabird SMP MicroCAT	7314	2152
Long Ranger ADCP	3301	2803
Nortek acoustic current meter	6275	3402
Seabird SMP MicroCAT	7315	3402
Nortek acoustic current meter	6276	3600
Seabird SMP MicroCAT	7316	3600

a. Data collection

Six full-depth moorings were deployed in the western Scotia Sea for the period 12 December 2009–5 December 2010 (Fig. 1a). The array, measuring 10.5 km × 10.5 km, was located just to the south of the mean position of the SAF (Orsi et al. 1995). To investigate the interaction between ACC flows and small-scale topography, the instruments were installed over a 700-m-tall topographic hill, with the minimum ocean depth occurring 3 km to the south of the C mooring. Streamlines derived from mean altimetry show a northeastward-directed ACC at this location; the same mean orientation was observed using the uppermost current meters (Fig. 1b).

The moorings comprised a series of paired current meters and Seabird MicroCAT instruments (measuring temperature, pressure, and salinity) at different depths, with the most heavily instrumented C mooring having 12 such pairs (Table 1). Unfortunately, owing to a large mooring knockdown event in late January 2010, both the northeast (NE) and southwest (SW) moorings suffered an implosion of buoyancy, so they only collected usable data until 27 January and 3 February, respectively. In addition, the bottom current meter on the southeast (SE) mooring was lost. On account of this, the analysis in this paper predominantly uses data from the center (C) mooring. After data recovery, a series of processing steps developed initially for the North Atlantic RAPID array was carried out as quality control (Collins et al. 2008). For both the current meters and MicroCAT instruments, deployment and recovery periods were removed and obvious spikes were identified and flagged. Each MicroCAT was attached to a CTD frame and dipped using extended bottle stops, in order to assess the offset between the conductivity cell on the MicroCAT and the bottle-calibrated CTD cell. In the case of the current meters, magnetic declination and speed of

sound corrections were made, and spikes were removed using a 10-fold factor routine.

The C mooring was also equipped with a downward-looking RD Instruments Long Ranger ADCP, nominally ensonifying the depths between 2803 and 3400 m. With this instrument, u and v velocities were measured in 37 16-m bins, with 11 evenly spaced pings per ensemble (ensemble length 30 min). Here, 500 m of good data were typically obtained. Data with a percentage-good value of less than 50%, based on low correlations and large error velocities, were discounted, though the magnitude of the observed shear variances (section 3b) did not significantly change depending on the threshold used (both 25% and 75% were tested).

Given a typical buoyancy frequency of $1.6 \times 10^{-3}\,\mathrm{s}^{-1}$, the Brunt–Väisälä period is ~10.5 min and the inertial period at 56°S is 14.4 h. Thus, the sampling rate of 15 min used for the MicroCAT instruments and current meters captures the majority of the internal wave field. Battery constraints necessitated a longer sampling interval of 30 min for the ADCP.

During mooring recovery, a multibeam bathymetry survey of the region was conducted using the echosounder multibeam (EM) 120 system installed onboard Royal Research Ship (RRS) *James Cook*. Data were cleaned using a combination of automatic and manual processing options (Meredith 2011). The final bathymetry output was a gridded surface with a horizontal resolution of 50 m.

b. *Current meter and MicroCAT filtering and processing*

After experimentation with a number of frequency cutoffs, three time series of the current meter and MicroCAT data were produced. The first is a simple 40-h low-pass Butterworth filter (sixth order) designed to remove near-inertial and diurnal/semidiurnal tidal activity; time series of these quantities are displayed in Fig. 2. When comparing the ADCP shear variance time series (section 3b) with subinertial current speed (section 3c), the filter was modified to be a bandpass from 40 h to 90 day [similar to that used by Phillips and Rintoul (2000)]. This filtering range also removes the long-term background mean flow associated with meanders and large-scale movements of the fronts. Finally, unfiltered versions of these time series are used in the spectral and wavelet analysis (sections 3d,e). Both the low- and bandpass filtered time series were subsampled at 1-day resolution.

Given the periodic large knockdown of the C mooring (up to 800 m for the top instruments and 80 m for the near-bottom instruments), consideration had to be given to the effect of these motions on the MicroCAT and current meter time series. A scheme of mooring motion correction was implemented based on the methods developed by Hogg (1986, 1991) and modified by Cronin et al. (1992). Canonical relationships between temperature/pressure and salinity/pressure were established using 40-h low-passed versions of all C mooring MicroCAT data, with curve fitting using a third-order polynomial (a spline fit was also trialed). Temperature and salinity were then interpolated onto nominal instrument levels using the two nearest instruments (in pressure space), the polynomial relationships, and an inverse-distance weighting scheme, as follows (for temperature):

$$T_{c_p} = w_1(T_{\mathrm{can}_p} - T_{\mathrm{can}_{p_1}} + T_{\mathrm{meas}_{p_1}}) + w_2(T_{\mathrm{can}_p} - T_{\mathrm{can}_{p_2}} + T_{\mathrm{meas}_{p_2}}), \quad (1)$$

where T_{c_p} is the corrected temperature at the nominal instrument pressure p, T_{can_p} is the canonical temperature at the nominal pressure, $T_{\mathrm{can}_{p_{1,2}}}$ is the canonical pressure at the level of instrument (either 1 or 2), $T_{\mathrm{meas}_{p_{1,2}}}$ is the measured temperature at instrument 1 or 2, and $w_{1,2}$ are the inverse distance weights for the instrument 1 or 2. Here, u and v were corrected using the vertical gradient in specific volume anomaly between the nominal instrument pressure and the two nearest current meter/MicroCAT pairs, as follows:

$$u_{c_p} = \frac{u_{r_1}(\delta_{c_p} - \delta_{\mathrm{meas}_2}) + u_{r_2}(\delta_{\mathrm{meas}_1} - \delta_{c_p})}{\delta_{\mathrm{meas}_1} - \delta_{\mathrm{meas}_2}}\cos(\theta) - v_{r_1}\sin(\theta) \quad (2)$$

and

$$v_{c_p} = \frac{u_{r_1}(\delta_{c_p} - \delta_{\mathrm{meas}_2}) + u_{r_2}(\delta_{\mathrm{meas}_1} - \delta_{c_p})}{\delta_{\mathrm{meas}_1} - \delta_{\mathrm{meas}_2}}\sin(\theta) + v_{r_1}\cos(\theta), \quad (3)$$

where δ is the specific volume anomaly ($\mathrm{m}^3\,\mathrm{kg}^{-1}$), θ is the direction of mean shear between the two nearest current meters, and u_{r_1} and v_{r_1} are the velocities at the nearest current meter rotated into the shear coordinates.

The accuracy of corrected T, S, u, and v was tested by withholding MicroCAT and current meter data at one pressure level and evaluating root-mean-squared (rms) differences between the values predicted using the motion correction scheme and the actual values at that level. Significant reductions in rms error were found to occur by using the corrected values as opposed to using simply the nearest current meter in space; these improvements were particularly large in the near-surface instruments (e.g., the rms difference in temperature for the 400 m instrument was reduced from 0.14° to 0.11°C,

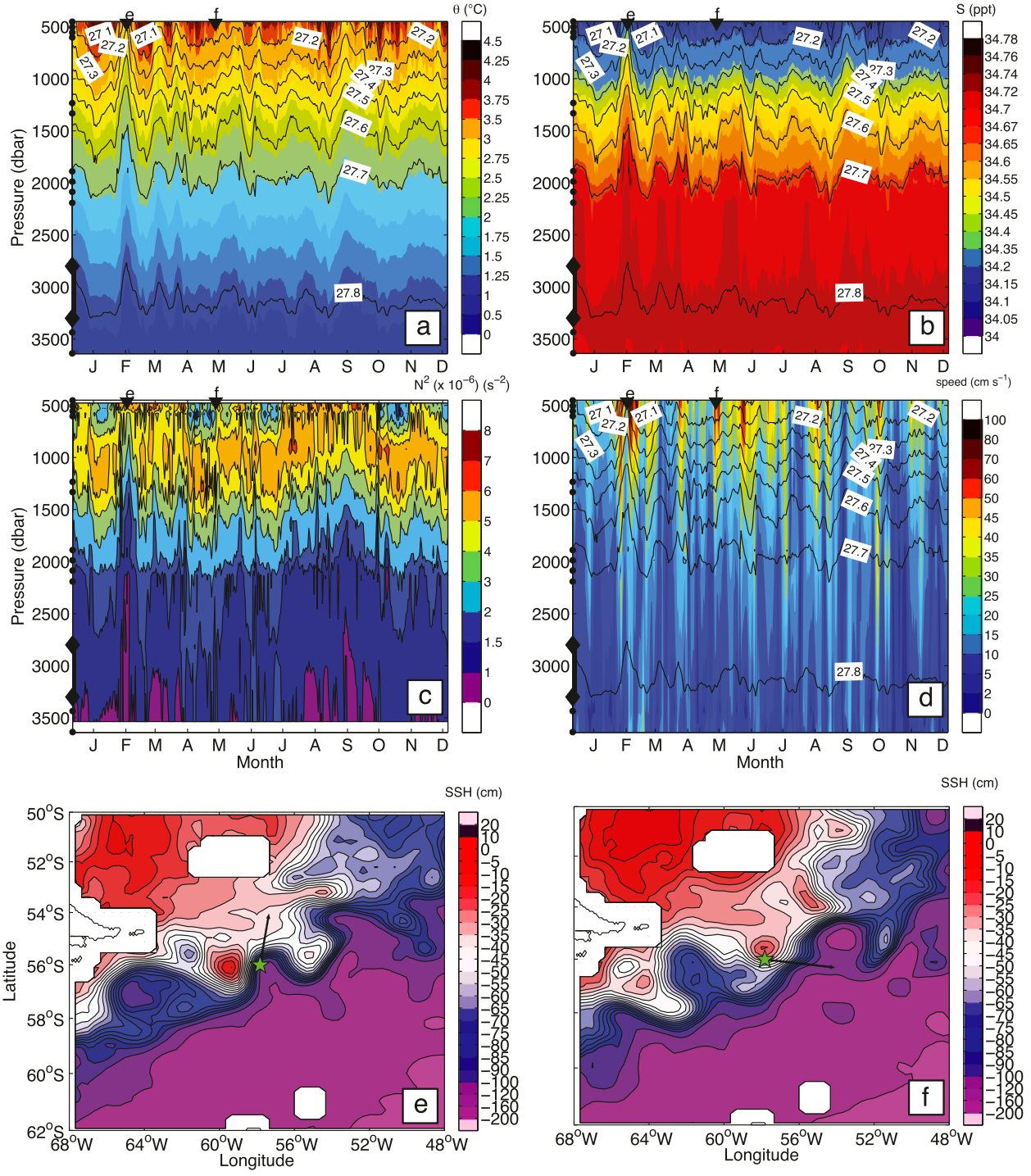

FIG. 2. Time series of (a) potential temperature (°C), (b) salinity, (c) N^2 ($\times 10^{-6}$ s^{-2}), and (d) current speed (cm s^{-1}), in color. Potential density contours (kg m^{-3}) are overlaid in (a),(b),(d). Mooring data were low-pass filtered at 40-h and subsampled at 1 day. The positions of the MicroCAT/current meter pairs are shown with black circles and the range of the ADCP is indicated with black diamonds. Daily altimetric snapshots (as in Fig. 1) for (e) 2 Feb 2010 and (f) 17 Apr 2010, when the array is south and north of the SAF alongside mean current vectors from the 453-dbar current meter on the C mooring on those days. The times of these snapshots are marked in (a)–(d).

and for u it was reduced from 6 to 4 cm s^{-1}). However, no improvement in rms error was observed below 2200 m, largely because of the weak vertical temperature and salinity gradients in this depth range. For this reason, the two deepest current meters (at ~3434 and ~3637 dbar) were not corrected using the scheme. Furthermore, given that the velocity correction assumes geostrophy, u and v velocities were not corrected for the evaluation of u and v spectra or tidal velocities, where we are interested in changes on internal wave time scales (sections 3d,e).

c. TKE dissipation estimates from moored ADCP data

Several studies (e.g., Naveira Garabato et al. 2004; Waterman et al. 2013a; Sheen et al. 2013) have used lowered ADCP data to infer the rate of TKE dissipation ε using finescale parameterization schemes. The theory underpinning these methods is reviewed by Kunze et al. (2006) and Polzin et al. (2013, manuscript submitted to *Rev. Geophys.*) and relies on the assumption that centimeter-scale dissipation can be quantified by measuring internal wave shear using a downscale energy cascade. Here, ε is estimated from the ratio of the observed energy density in the wave field to that of the Garrett and Munk (1976) internal wave model, expressed in terms of the integrated shear variance normalized by the buoyancy frequency $\langle V_z/\overline{N}\rangle^2$ and the accompanying GM value $\langle V_{z_{\rm GM}}/N_0\rangle^2$. In this notation, the angle brackets indicate the integration of the variance of the contained quantity between two specified vertical wavenumbers. Following Henyey et al. (1986) and Gregg et al. (2003),

$$\varepsilon = \varepsilon_0 \frac{f}{f_0} \frac{\cosh^{-1}(N/f)}{\cosh^{-1}(N_0/f_0)} \frac{\langle V_z/\overline{N}\rangle^2}{\langle V_{z_{\rm GM}}/N_0\rangle^2} h_1(R_\omega), \qquad (4)$$

where $\varepsilon_0 = 7.8 \times 10^{-10}$ W kg^{-1} is the background turbulent dissipation of a GM internal wave spectrum at latitude 30° in stratification $N_0 = 5.24 \times 10^{-3}$ rad s^{-1} (Garrett and Munk 1975). Absolute values of the Coriolis parameter at the latitude of interest (56°S) and at 30° are f and f_0, these being 1.2×10^{-4} s^{-1} and 7.3×10^{-5} s^{-1}; $h_1(R_\omega)$, which accounts for the dominant frequency in the observed wavefield, is defined as

$$h_1(R_\omega) = \frac{3(R_\omega + 1)}{2\sqrt{2}R_\omega\sqrt{R_\omega - 1}} \qquad (5)$$

and is a function of the shear-to-strain ratio R_ω (Polzin et al. 1995), set at 4.5 in this study (see below). Its value for $R_\omega = 4.5$ is 0.69.

To obtain $\langle V_z/\overline{N}\rangle^2$, each quality-controlled velocity profile of the Long Ranger ADCP (17 232 in total over 360 days) was first differenced and divided by a time-dependent $\overline{N}$ (estimated from the MicroCAT instruments located at ~2050 and ~3400 m, respectively), where the overbar represents a vertical average (N values are linearly interpolated in time onto a 30-min time base). This normalized shear was then Fourier transformed (32 points) to yield the vertical wavenumber power spectral density. Consideration was given to the problems of spatial averaging inherent in ADCP data, discussed in relation to LADCP data by Polzin et al. (2002) and to mooring data by Damerell et al. (2011). Corrections for range averaging and finite differencing were made, but corrections for both tilt and beam separations were considered to be undesirable given the relatively small ADCP tilts (<2°) and our lack of knowledge about the horizontal wavenumber spectrum. In any case, application of the tilt correction yielded a change of $<5 \times 10^{-11}$ W kg^{-1}, which is below the noise floor of the instrument.

Some comments about ADCP noise and choice of shear spectrum integration limits are warranted. According to the Long Ranger literature, the error velocity in good scattering conditions scales according to 3.0 cm s^{-1} $n^{-0.5}$, where n is the number of pings per bin (http://www.rdinstruments.com). As each ensemble contains 11 pings, the error velocity for each shear measurement would thus be ~0.9 cm s^{-1}. However, a marked increase in spectral level was observed at high wavenumber, even in the absence of the spectral corrections, implying that the actual noise was larger than this value, in line with the conclusions reached by Kunze et al. (2006). Investigation of different noise levels suggested that the likely mean value was 6.0 cm s^{-1} $n^{-0.5}$, as a noise spectrum of this magnitude intersects the point at which mean clockwise and counterclockwise variances become distinctly different. Owing to the relatively high noise level, the wavelength integration limits for $\langle V_z/\overline{N}\rangle^2$ were chosen conservatively as 130 and 320 m.

In the absence of concurrent CTD strain data, a shear-to-strain ratio (i.e., R_ω) of 4.5 was used to estimate ε. This estimate is based on the mean R_ω calculated from ADCP shear and CTD strain data at 2800 to 3400 m collected at 18 stations in the region during mooring recovery. The standard deviation was 2.15, yielding 1σ maxima and minima of 6.6 and 2.3, respectively. Varying R_ω between 2.3 and 6.6 causes mean ε to vary from 1.09×10^{-9} to 2.83×10^{-9} W kg^{-1}. In addition, there is some evidence that the parameterization itself might overestimate ε in the ACC by up to a factor of 10 when compared with concurrent microstructure data, in the near-bottom region of high wave energy (Waterman et al. 2013b, manuscript submitted to *J. Phys. Oceanogr.*). For this reason, much of the forthcoming analysis focuses on $\langle V_z/\overline{N}\rangle^2$, which captures the temporal variability in

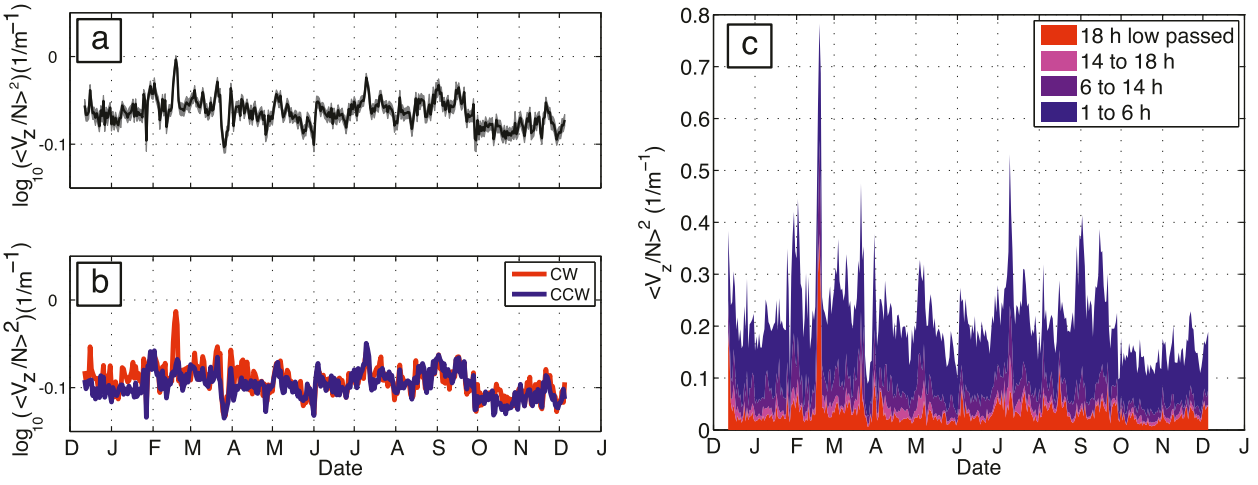

FIG. 3. (a) Daily time series of $\langle V_z/\overline{N}\rangle^2$, the buoyancy frequency–normalized shear variance, integrated between 130- and 320-m wavelengths (for a nominal depth range of 2803–3400 m). Here, 90% confidence intervals calculated by bootstrapping are overlaid; (b) the time series is divided into CW (upward propagating) and CCW (downward propagating) components; and (c) as in Fig. 3a, but for shear variance divided into different frequency bands.

mixing (see section 3b) but is not reliant on the accuracy of the parameterization [see Kunze et al. (2002) and Klymak et al. (2008) for examples of regions where finescale methods can underestimate the real value of turbulent dissipation].

As the parameterization assumes a stationary internal wave field and the individual 30-min resolution $\langle V_z/\overline{N}\rangle^2$ profiles are noisy, it was decided to average together spectra over 1 day when compiling time series of $\langle V_z/\overline{N}\rangle^2$ and ε. However, for the wavelet analysis in section 3e, a 2-h averaging interval was used.

d. *Satellite altimetry*

Sea surface height anomalies were obtained from the delayed-time gridded $\frac{1}{3}° \times \frac{1}{3}°$ AVISO product (http://www.aviso.oceanobs.com/en/data/products/sea-surface-height-products/global/msla.html#c5122). These estimates were linearly interpolated onto a daily time base to coincide with the daily subsampled mooring measurements, before the addition of mean sea level height obtained from Maximenko et al. (2009) to yield absolute SSH.

3. Results

a. *Hydrographic, altimetric, and velocity observations*

The 40-h low-pass-filtered time series of potential temperature θ, salinity S, N^2, and current speed at the C mooring are shown in Figs. 2a–d. Low-frequency temperature and salinity changes are largely governed by the north–south movement of the SAF, clearly visible in altimetry (Figs. 2e,f show examples of times when the mooring is located to the south and north of the front, respectively). The mooring is located to the north of the SAF until 25 January, when a large northward meander moves cold water across the array in concert with a strong jet (Figs. 2a,b,d). Warm north-of-front conditions prevail until mid-August, when a large detached eddy again causes a jet to transit across the array, bringing cold water northward. The mooring is then positioned to the north of the SAF from October to the end of the deployment. At times when the front moves to the north of the array, stratification over most of the water column is weaker (Fig. 2c), with near-surface N^2 values typically reducing from $\sim 6 \times 10^{-6}$ to $4 \times 10^{-6}\,\mathrm{s}^{-1}$. This frontal movement is the dominant control on temperature variability at the mooring site, with equivalent barotropic fluctuations being the leading empirical orthogonal function of temperature, representing 79% of the total variability.

Maximum current speeds exceed $70\,\mathrm{cm\,s}^{-1}$ above 1000 m and the flow down to 3000 m has equivalent barotropic structure typical of ACC jets. Nevertheless, there are periods with pronounced near-bottom flow, with 23 days having mean 3637 dbar speeds exceeding $15\,\mathrm{cm\,s}^{-1}$. Interestingly, the periods of strongest near-bottom flow do not typically coincide with times of high near-surface speed. This observation is discussed further in section 3c.

b. *Time series of integrated shear variance and estimated TKE dissipation*

The daily time series of buoyancy-normalized shear variance $\langle V_z/\overline{N}\rangle^2$, integrated between 130- and 320-m wavelengths, is presented in Fig. 3a (hereafter referred to simply as shear variance). High shear variance levels

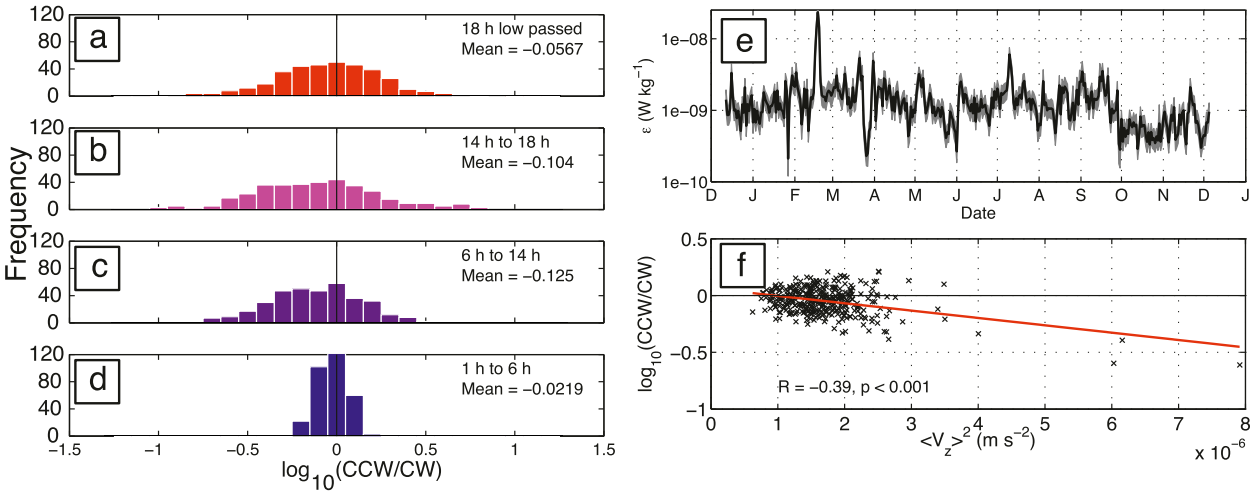

FIG. 4. (a)–(d) Histograms of rotary coefficient by frequency band with mean values in each band displayed; (e) time series of turbulent dissipation ε (W kg^{-1}) calculated using Eq. (4); and (f) $\langle V_z \rangle^2$ plotted against rotary coefficient with best-fit linear regression line plotted.

are observed during February–April, mid-July, and late August–September; variance is notably reduced in June and October–November. The mean (median) rotary coefficient [$\log_{10}$(CCW/CW)], which expresses the ratio of counterclockwise (CCW) to clockwise (CW) variance, is −0.048 (−0.040), with an accompanying two standard error confidence interval of 0.015. This indicates a dominance of clockwise, upward-propagating internal wave energy, presumably radiated from the sea floor (Fig. 3b). The very large peak in $\langle V_z/\overline{N} \rangle^2$ in mid-February 2010 is attributable to a pronounced maximum in upward energy propagation at this time. Further evidence that the energy propagation is predominantly upward is shown later (see Fig. 6, described in greater detail below).

A frequency decomposition of the time series is displayed in Fig. 3c. Here, ADCP velocities have been bandpass filtered at different periods to separate high-frequency internal waves (periods of 1–6 h), dominant semidiurnal tidal frequencies (6–14 h), near-inertial waves (14–18 h), and subinertial motions (>18 h). Total shear variance is dominated at all times by internal wave frequencies, with periods shorter than 18 h (which includes the near-inertial band) contributing 85% of the total variance and wave bands shorter than 6 h constituting over 63% of the total. Lower-frequency motions (>18 h) only occasionally contribute larger fractions of the total variance, such as during the notable shear variance maximum on 18 February.

The frequency decomposition for clockwise and counterclockwise components independently (Figs. 4a–d) shows that, while total shear variance is dominated by high-frequency motions, the excess of upward-propagating energy is found primarily as lower-frequency internal waves and in the near-inertial band (i.e., at 6–18 h). The mean value of rotary coefficient for periods shorter than 6 h is −0.022 (±0.001), indicating only weak polarization, while the mean value for periods between 6 and 18 h is −0.12 ± 0.02.

To understand the upward propagation of energy more clearly, the ADCP velocities were carefully examined. Rotary spectra of these velocities in frequency space (Fig. 5) show a strong counterclockwise rotation in time (centered on f), owing to the direction of inertial motions in the Southern Hemisphere. The 6-h low-pass-filtered u velocity anomalies for a 20-day period in March/April 2010 are displayed in Fig. 6a; these exhibit

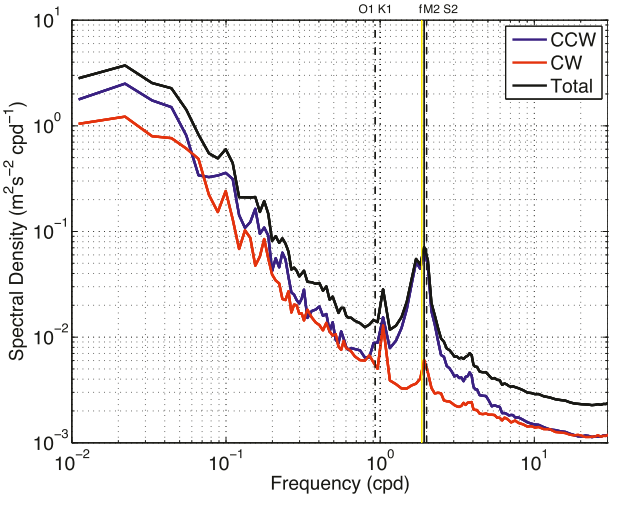

FIG. 5. Rotary spectra of depth-averaged ADCP velocity for 12 Dec 2009–5 Dec 2010. Diurnal and semidiurnal tidal frequencies and the inertial frequency are marked.

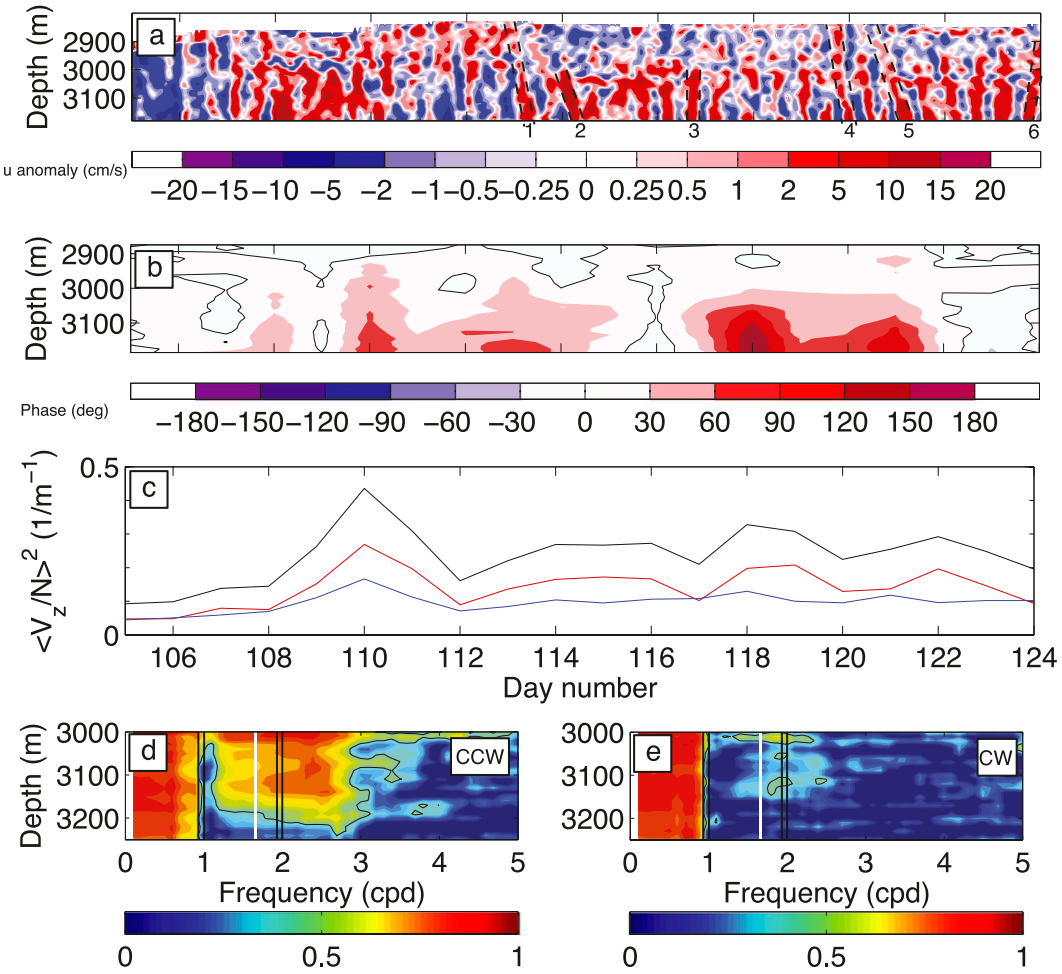

FIG. 6. (a) The 6-h low-pass-filtered geographical u velocity anomaly (relative to the depth-mean u for each ADCP ensemble) for the period 16 Mar–4 Apr 2010 for the depth range 2800–3200 m. Periods of downward phase shift are shown with dashed lines with labels 1, 2, 4, and 5. Periods of no or upward phase shift are shown with dashed lines and labels 3 and 6. (b) CCW-rotating velocity phase shift at 6-h period between adjacent depth bin of the ADCP and cumulated downward from the uppermost bin. The dominant positive phase shift with increasing depth implies a downward internal wave phase propagation, and thus an upward energy propagation; (c) $\langle V_z/\overline{N}\rangle^2$ for the same period, with CW and CCW components in red and blue respectively; (d) coherence of CCW-rotating velocities for the same time period. The area surrounded by the black line indicates statistical significance at 95%; and (e) as in Fig. 4d, but for CW velocities.

evidence of downward internal wave phase propagation (at times indicated by the numbers 1, 2, 4, and 5). This propagation is shown more explicitly in Fig. 6b, which displays phase shifts of the dominant counterclockwise-rotating component in velocity between different ADCP bin depths. Periods of strong clockwise wavenumber shear (Fig. 6c) exhibit a positive phase shift relative to shallower levels (Fig. 6b). This is particularly pronounced between days 110 and 115 and between days 118 and 122. This downward internal wave phase propagation is indicative of upward energy propagation from the bottom. In contrast, times of relatively weak shear polarization (e.g., days 116 and 124) do not exhibit the strong positive phase shift with depth (Fig. 6b) and have either no (label 3) or slight upward (label 6) phase propagation.

The vertical coherence of the counterclockwise-rotating velocity components (in time) is shown in Fig. 6d. Statistically significant coherence is observed at subinertial frequencies (<1 cpd) and at periods between the near-inertial and 3 cpd. In contrast, no significant coherence in counterclockwise-rotating components is observed beyond 3 cpd. This result corroborates that previously discussed for the vertical wavenumber shear (Figs. 4a–d), which found that upward energy propagation occurred primarily in the 6–18-h band. The corresponding figure for the (much weaker) clockwise-rotating velocity

TABLE 2. Correlation coefficient between the raw integrated shear variance $\langle V_z \rangle^2$, normalized integrated shear variance $\langle V_z/\overline{N} \rangle^2$, TKE dissipation rate ε estimated from the finescale parameterization, buoyancy frequency N, geopotential anomaly at 453 dbar relative to 3637 dbar δ, and rotary coefficient (RC). Correlations that are significant at the 5% level (after an autocorrelation analysis to compute the effective degrees of freedom) are highlighted in boldface.

	$\langle V_z/\overline{N} \rangle^2$	ε	N	δ	RC
$\langle V_z \rangle^2$	**0.93**	**0.82**	−0.01	−0.09	**−0.25**
$\langle V_z/\overline{N} \rangle^2$	—	**0.94**	−0.33	−0.37	**−0.25**
ε	—	—	0.001	−0.10	**−0.39**
N	—	—	—	**0.87**	−0.23
δ	—	—	—	—	−0.14

components is shown in Fig. 6e and exhibits no significant coherence at periods shorter than 1 cpd.

Using $R_\omega = 4.5$ yields a mean ε of $1.46 \times 10^{-9}\,\mathrm{W\,kg^{-1}}$ (Fig. 4e). Daily values of ε vary by roughly two orders of magnitude, from 2.11×10^{-10} (27 January) to $2.34 \times 10^{-8}\,\mathrm{W\,kg^{-1}}$ (18 February). While not an independent estimate at the same time, the mean value of dissipation at the mooring location is in approximate agreement with dissipation rates inferred from lowered ADCP and CTD measurements collected after the moorings were recovered in December 2010 (Sheen et al. 2013).

As discussed in section 3a, the stratification of the water column decreases significantly at times when the mooring is located to the south of the SAF. Before analyzing the impact of mesoscale motions on shear variance, it is useful to understand the relative contributions of changes in stratification and shear to the time series of ε. To do this, correlations were calculated between raw shear variance $\langle V_z \rangle^2$ (i.e., without N normalization), the buoyancy frequency N, and ε (Table 2). As a separate measurement of cross-frontal position, the geopotential anomaly (δ; $\mathrm{J\,kg^{-1}}$) at 453 dbar relative to 3637 dbar (i.e., the surface MicroCAT relative to the deepest) was also computed for each day and correlated with the other quantities. Significant and strong correlations were obtained between $\langle V_z/\overline{N} \rangle^2$ and $\langle V_z \rangle^2$ and between ε and $\langle V_z \rangle^2$, suggesting that the variability encapsulated in Fig. 3a is being strongly driven by changes in the velocity field. In contrast, the correlations between $\langle V_z/\overline{N} \rangle^2$ and N and between ε and N are weak, implying that stratification is not the dominant control on mixing. Furthermore, no significant correlations were observed between δ, which is relatively large when the mooring is to the north of the SAF, and any of the shear variance measures. However, it is worth noting that changes in shear are quantified much more precisely than those in stratification (a single depth-averaged N is acquired at each time step and a constant R_ω is used when determining ε).

In common with results obtained by Damerell et al. (2011), a statistically significant correlation is observed between the rotary coefficient [$\log_{10}$(CCW/CW)] and both measures of normalized shear variance and ε (Fig. 4f). This suggests that instances of particularly strong dissipation are associated with enhanced upward energy propagation, implying that bottom-sourced internal wave generation is important at this location. However, it should be remarked that much of this positive correlation is accounted for by a handful of strong clockwise-polarized high dissipation events (centered on, for example, 15 December 2009 and 21 March 2010). This relationship is discussed further in section 4b.

c. *Empirical relationship between subinertial flows and enhanced shear variance*

As already outlined, several previous studies have postulated that the amplitude of the internal wave field is modulated by subinertial eddy activity, particularly where near-bottom flows are large [$O(10\,\mathrm{cm\,s^{-1}})$]. Specifically, it has been suggested that the impingement of equivalent barotropic jets on the topography generates enhanced mixing up to 1 km off the bottom within these features. In other regions (e.g., near midocean ridges), internal tides are thought to be the dominant source of shear variance. In this section, we analyze whether these ideas are applicable in the Scotia Sea.

A power spectrum of the shear variance time series is displayed in Fig. 7a. The spectra is strongly red, with modulation of shear variance occurring mostly at subinertial periods O(10 days). A modest tidal peak centered on the M_2 frequency is also discernible, which only just achieves significance at the 95% level when tested against a red noise model. This tidal peak arises from the differing strength of the internal tide between the different bin depths of the ADCP. Nevertheless this signal is relatively weak; a harmonic analysis of ADCP u and v velocities over the whole year reveals that the internal tidal signal is $\sim 0.3\,\mathrm{cm\,s^{-1}}$ at the bin nearest the transducer face and only $\sim 1.0\,\mathrm{cm\,s^{-1}}$ at a nominal depth of 3120 m (Fig. 7b). Furthermore, all of the subinertial part of the spectrum at periods longer than 2–3 days is statistically different than the red noise model, suggesting that the shear variance is modulated primarily on eddy time scales. No significant peak at 14-day periods (evidence of a spring–neap cycle) can be observed, though we note that this does overlap with eddy periods so does not on its own preclude spring–neap modulation. The direct correlation between barotropic tidal velocities and $\langle V_z/\overline{N} \rangle^2$ is discussed in more detail in section 3e.

To quantify the influence of eddy flows, daily values of $\langle V_z/\overline{N} \rangle^2$ from the ADCP were correlated with 40-h–90-day bandpass-filtered current speeds from the 12

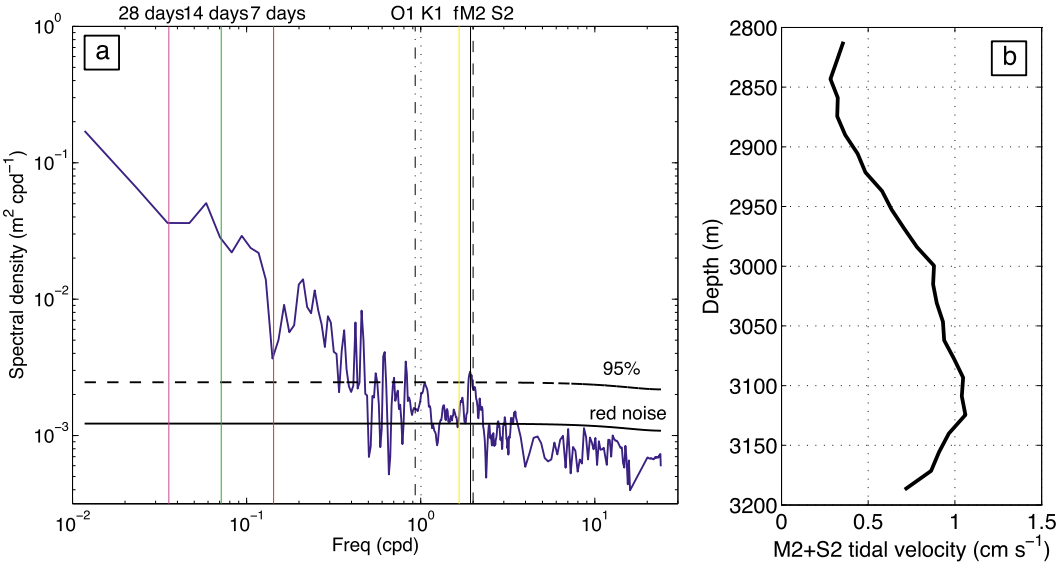

FIG. 7. (a) Power spectrum (Welch estimate with 8 overlapping windows) of $\langle V_z/\overline{N}\rangle^2$. The dominant tidal frequencies and the inertial frequency are marked. A red noise spectrum [based on an autoregressive 1 (AR1) model] is plotted, with the 95% upper confidence limit as a dashed line. For frequencies greater than 0.8 cpd, 10 spectral points are averaged. (b) Max amplitude of $M_2 + S_2$ tidal velocity derived from harmonic analysis of ADCP time series. A weak baroclinic tidal signal can be seen.

current meters on the C mooring (Fig. 8a). The correlations between bottom-current speed and clockwise- and counterclockwise-polarized shear are also shown, along with correlations between $\langle V_z/\overline{N}\rangle^2$ and bandpass-filtered ADCP velocities at each bin depth (inset panel). The regression relationship for the bottom-most current meter is shown in Fig. 8b.

A maximum in correlation ($r = 0.45$) between $\langle V_z/\overline{N}\rangle^2$ and current speed is observed close to the bottom, with much smaller (and insignificant) correlations above 2500 m and slightly negative (but insignificant) correlation in the near-surface current meters. For the two current meters that resided beneath the ADCP (at ~3400 and 3600 m), correlations were largest for the upward-propagating component. To elucidate further the flow structure associated with periods of enhanced shear variance, daily current speed profiles are plotted in Fig. 8c alongside mean profiles for the 180 days with the largest and smallest shear variances. No significant difference is observed in the near-surface current speeds, implying that enhancement of $\langle V_z/\overline{N}\rangle^2$ is not associated with an equivalent-barotropic increase in speed at all levels. Instead, only current speeds below 2000 m are increased, with particularly strong flow enhancement near the bottom. Similar analyses for both upward- and downward-propagating energy (not shown) yield near-identical results. The robustness of the analysis was tested using different numbers of ranked days (e.g., the 90 days with the highest and lowest shear variances); in each case the result remained qualitatively similar.

Given the depth dependence of the relationship between current speed and $\langle V_z/\overline{N}\rangle^2$, EOFs of the bandpass-filtered speed time series were calculated and the resulting amplitudes tested for correlation with the shear variance time series (Fig. 9). While EOF1 (the equivalent barotropic mode) explains over 62% of the speed variance, its amplitudes are not significantly correlated with the time series of $\langle V_z/\overline{N}\rangle^2$ (Figs. 9a,b). In contrast, the amplitudes of EOF2 (the first baroclinic mode with a zero crossing near 1500 m) have a statistically significant correlation with $\langle V_z/\overline{N}\rangle^2$ [$r = 0.36$, $p < 0.01$, and degrees of freedom (df) = 70; Figs. 9c,d]. A slightly weaker (though still significant) correlation is also observed with EOF3 ($r = 0.32$, $p < 0.01$, and df = 70; Figs. 9e,f). These correlations highlight the fact that enhanced shear variance is associated specifically with amplification of the near-bottom speeds.

In addition to the current speed, the direction of flow at times of high and low shear variance was also investigated. However, no correlation was found between the direction of the flow and $\langle V_z/\overline{N}\rangle^2$.

d. Influence of subinertial current speed on internal wave kinetic energy

In light of the marked increase in $\langle V_z/\overline{N}\rangle^2$ at times of strong subinertial near-bottom speeds, one might expect

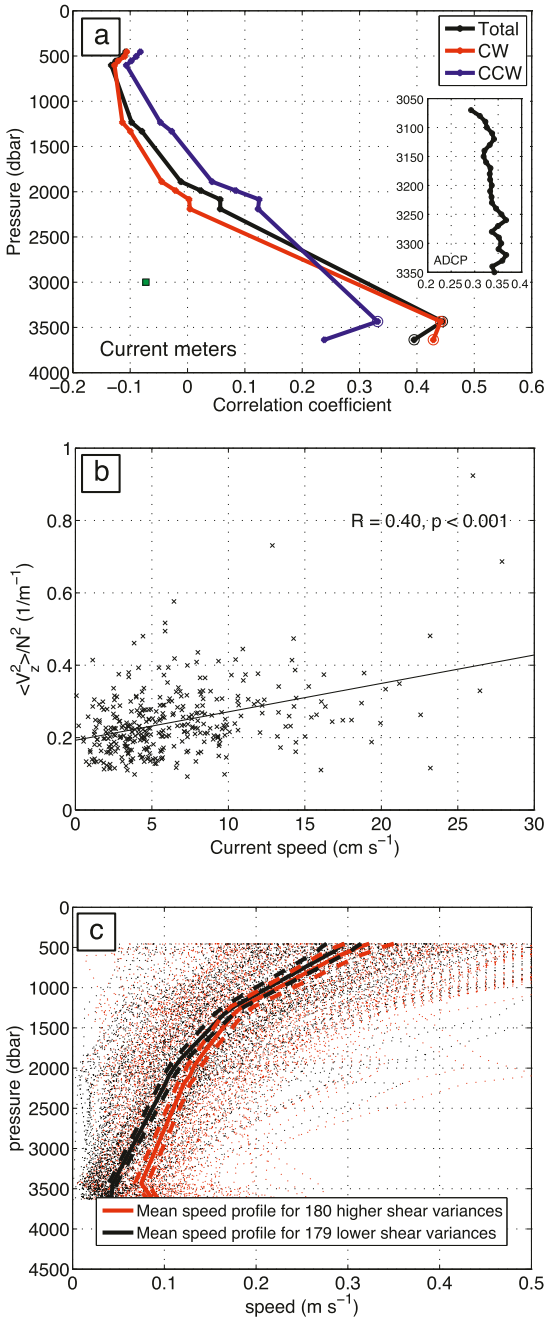

FIG. 8. (a) Correlation coefficient between daily time series of $\langle V_z/\overline{N}\rangle^2$ (and CW/CCW components) from moored ADCP at ~2800 m and 40-h–90-day bandpass-filtered current speed measured by 12 current meters on the C mooring. Correlations for which the p value is less than 0.05 have circular markers. Accompanying correlations for each bin of the ADCP are shown in the inset panel, while the correlation with barotropic tidal velocity is shown in green (details in text). (b) Regression relationship for $\langle V_z/\overline{N}\rangle^2$ vs bottom current meter speed at 3637 dbar; and (c) mean current speed profiles at the C mooring for the periods of 180 highest and 179 lowest $\langle V_z/\overline{N}\rangle^2$ values in red and black, respectively. Standard errors are given as thick dashed lines and each individual daily profile in thin dashed lines.

an accompanying increase in kinetic energy at internal wave frequencies. To test this hypothesis, the 360-day u and v time series from each current meter and from the ADCP was divided into overlapping 17-day segments and variance-preserving Welch power spectra were calculated of horizontal kinetic energy for each segment (8 Hamming windows with 50% overlap). For each spectrum, the variance was integrated in a number of frequency bands between 0.1 and 1.25 days, and this was correlated against the mean subinertial current speed U_0 at that depth level in the 17-day period. Results from this analysis are plotted in Fig. 10a. Mean spectra of horizontal kinetic energy of the bottom current meter (3637 dbar) for different background current speeds are shown in Fig. 10b.

The only statistically significant correlations observed between U_0 and horizontal kinetic energy occur in the bottom two current meters and the ADCP, where the strongest correlation occurs at near-inertial and high frequencies. In view of the analysis presented in section 3a, this would suggest an increase both in clockwise polarization (as near-inertial waves tend to be polarized) and in total dissipation (as the high-frequency waves contribute most of the observed shear variance). No statistically significant correlations are observed further up the water column. The pattern is confirmed by examining kinetic energy spectra for the bottom current meter sorted by subinertial current speed (Fig. 10b); this shows a clear enhancement of both near-inertial and high-frequency internal wave kinetic energy at times when current speeds exceed 13 cm s^{-1}.

e. *The influence of tides on the shear variance time series*

In addition to subinertial flows, it is also interesting to assess the extent to which $\langle V_z/\overline{N}\rangle^2$ is controlled by barotropic tidal forcing. Some variability in $\langle V_z/\overline{N}\rangle^2$ at tidal frequencies was previously identified, but no conclusive evidence for a spring–neap modulation could be identified. Here, this issue is discussed in more detail.

To quantify the barotropic tide, a depth-averaged u and v time series was calculated from the 12 current meters, and the dominant M_2 and S_2 tidal frequencies were isolated by harmonic analysis using the Matlab T_TIDE package (Pawlowicz et al. 2002). A time series of $M_2 + S_2$ amplitudes was then constructed using the output of the analysis, which showed a spring peak amplitude of 1.6 cm s^{-1} compared with a neap minimum of 0.1 cm s^{-1}. We note that these values are very small compared with the depth-averaged mesoscale currents (Fig. 2d); however it is possible that a small oscillatory forcing may be more effective at generating internal waves than a larger geostrophic flow. To test the effect

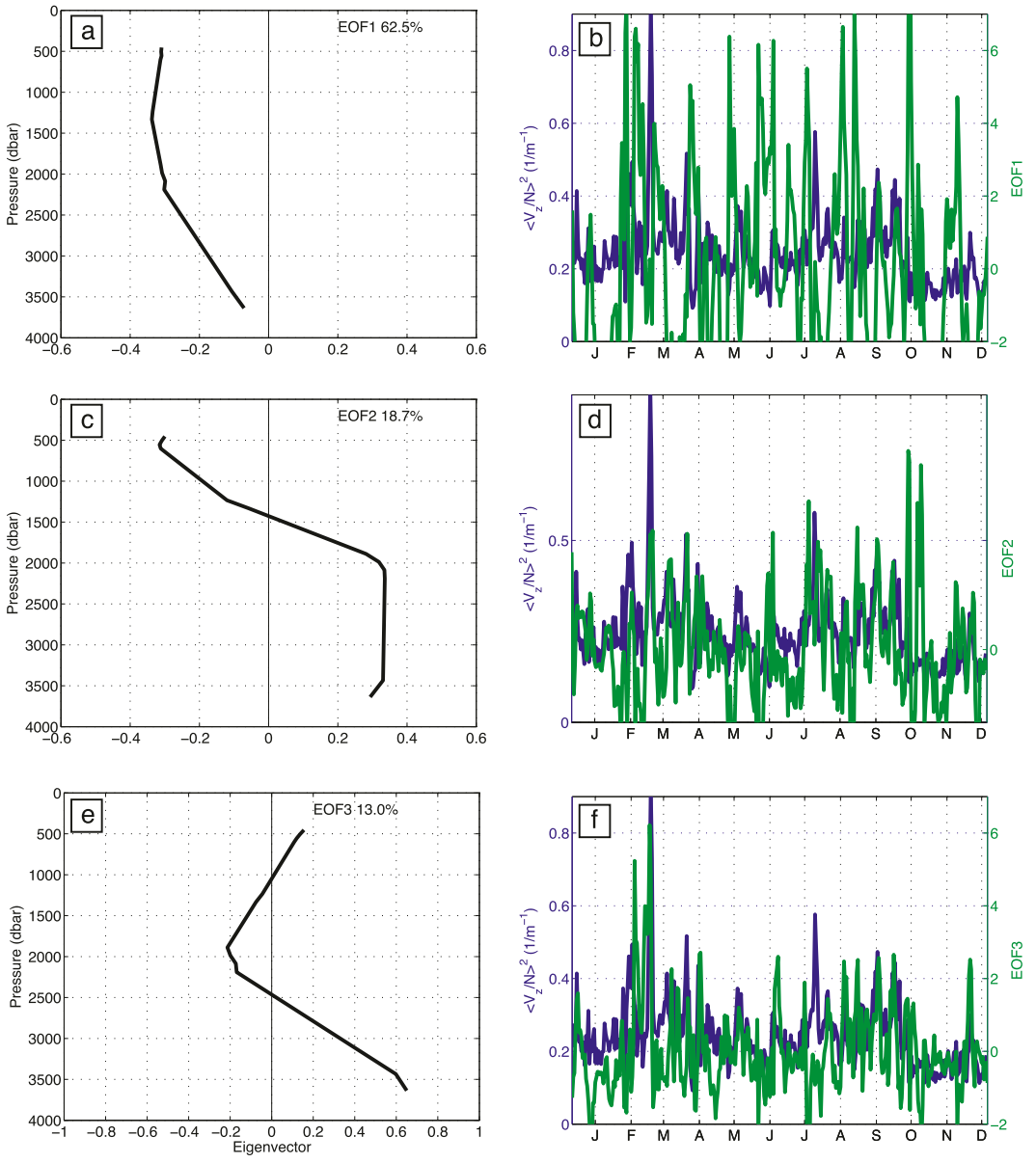

FIG. 9. (a) Vertical structure of EOF1 for 40-h–90-day bandpass-filtered current speed from 12 current meters on the C mooring; and (b) time series of amplitudes associated with EOF1 with $\langle V_z/\overline{N}\rangle^2$ overlaid. The correlation coefficient between the two series is 0.06 (not significant). (c) As in Fig. 9a, but for EOF2, and (d) as in Fig. 9b, but for EOF2. The correlation coefficient between the two series is 0.36. (e) As in Fig. 9a, but for EOF3, and (f) as in Fig. 9b, but for EOF3. The correlation coefficient between the two time series is 0.31.

of this spring–neap cycle on $\langle V_z/\overline{N}\rangle^2$, five-day-averaged rms $M_2 + S_2$ amplitudes were correlated with identically averaged $\langle V_z/\overline{N}\rangle^2$, as the continuum internal wave field is thought to evolve over these time scales. However, no significant correlation was found ($r = -0.07$, $p = 0.82$, plotted in Fig. 8a with green symbol). A similar correlation analyses was performed using the rms $M_2 + S_2$ amplitudes estimated for each 17-day time slice (15 days is the minimum period that can accurately distinguish these amplitudes). Once again, no significant correlation was observed ($r = 0.05$, $p = 0.83$), suggesting that the spring–neap cycle is unlikely to be a significant control on mixing rates at this location.

Further insight can be gained into the nature of the relationship between subinertial flows, tidal flows, and shear variance through wavelet analyses of bottom current meter speed (Fig. 11a) and $\langle V_z/\overline{N}\rangle^2$ (Fig. 11b). Strong variability on internal wave time scales is exhibited by

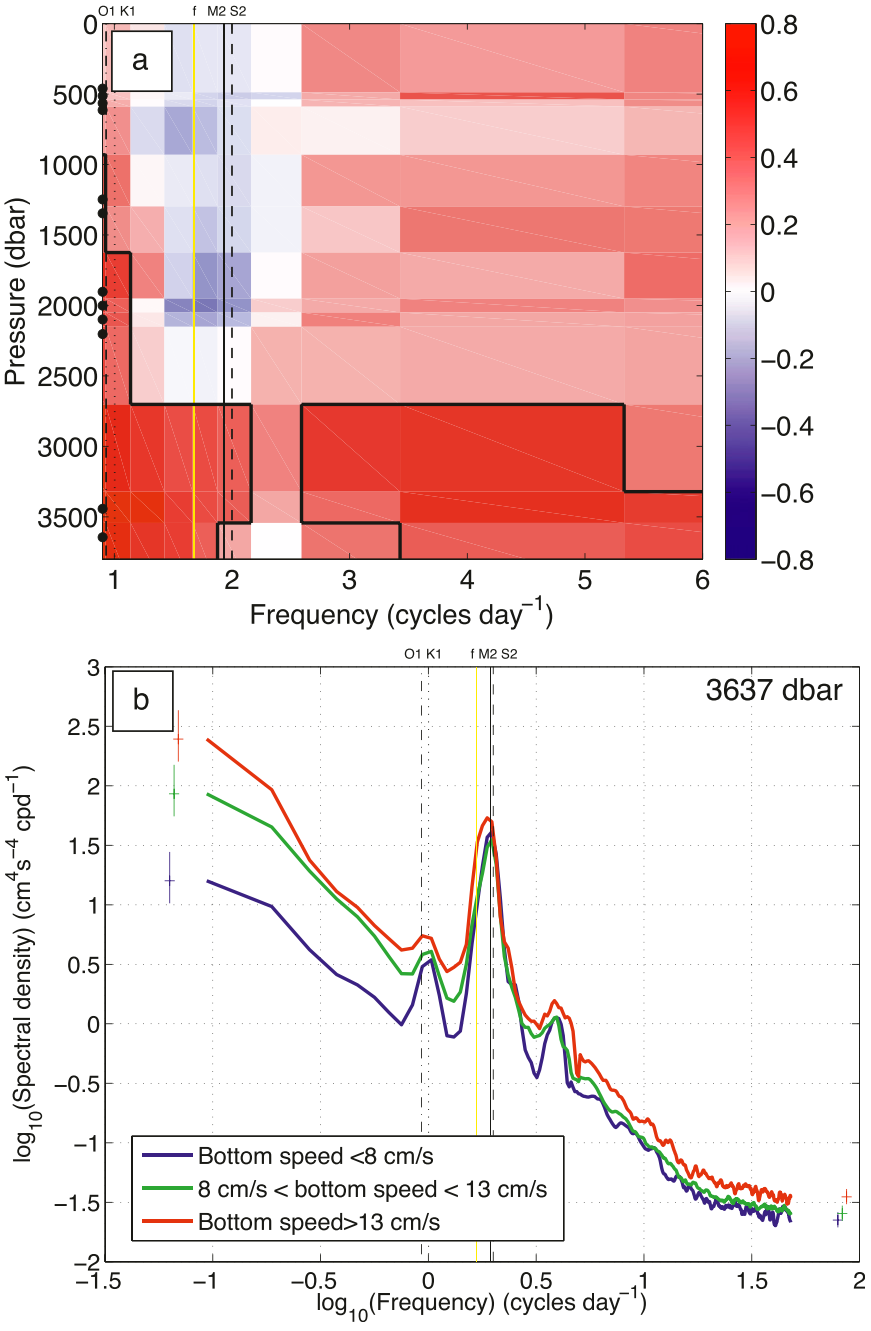

FIG. 10. (a) Correlation coefficients between integrated spectral density of KE in a number of frequency bands and 17-day mean subinertial current speed (overlapping 17-day segments, Welch spectral estimate, 8 Hamming windows) from current meters and the moored ADCP. Regions enclosed by black lines indicate areas where the correlation is significant at the 5% level; and (b) average kinetic energy spectrum $(u'' + v'')^2/2$ sorted by subinertial current speed. For frequencies greater than 0.7 cpd, 10 individual spectral estimates are averaged to reduce the error. The symbols at the left of the spectrum represent 95% confidence intervals for the spectra, assuming a χ^2 model, while the symbols on the right represent the same quantity for the averaged spectra for frequencies exceeding 0.7 cpd. Tidal and inertial frequencies are marked.

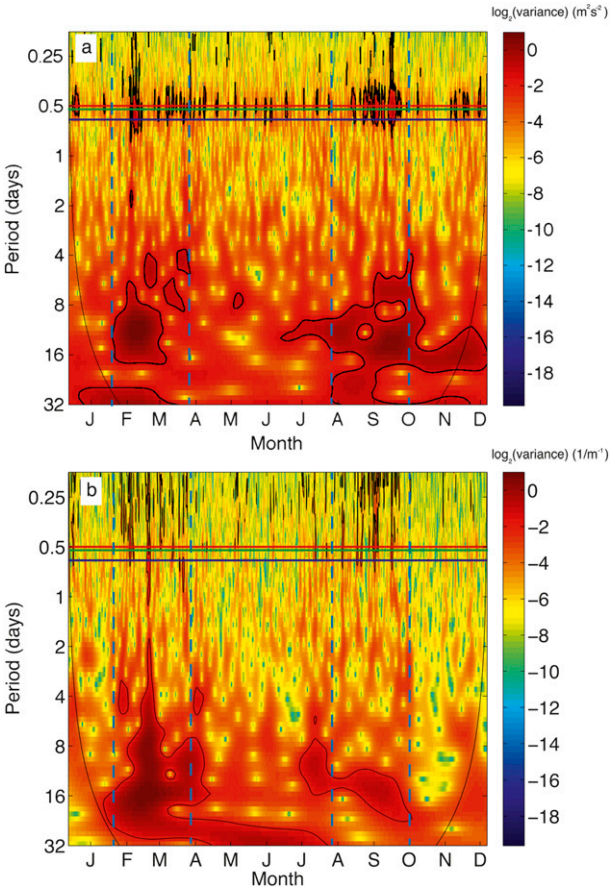

FIG. 11. Morlet wavelet spectra for (a) current speed at 3637 dbar on the C mooring, and (b) buoyancy-normalized shear variance $\langle V_z/\overline{N}\rangle^2$ from the Long Ranger ADCP integrated between 130 and 320 m. The areas surrounded by a solid contour indicate significance at the 95% level. The curved line indicates the cone of influence. The dashed lines indicate periods between mid-January and late-March and between early August and early October when the spectra is enhanced at both subinertial and superinertial frequencies. The red and green lines indicate semidiurnal tidal periods (S_2/M_2) and the blue line represents the inertial period.

$\langle V_z/\overline{N}\rangle^2$, particularly between late January and late March and between mid-July and early October. These periods coincide with times when modulation of current speed at 4–16-day periods is comparatively strong and also with times when semidiurnal tidal modulation is pronounced (Fig. 8a). While no significant correlation was found between rms values of tidal current speed and of five-day-averaged shear variance, this implies that high-frequency (i.e., periods less than 12 h) variability in $\langle V_z/\overline{N}\rangle^2$ may be more pronounced at times when there is strong modulation of subinertial flow speed and larger amplitude tidal velocities. The reasons for enhancement of tidal velocities at the same time as strong mesoscale variability are unclear, but the observation points to a coupling between tidal and subinertial flows in the area; possible mechanisms that could underpin such a coupling are discussed by, for example, Zaron et al. (2009).

4. Discussion

An empirical relationship has been established in which enhanced (and generally clockwise polarized) shear variance is modulated by subinertial near-bottom flow magnitude but is decoupled from flow intensification in the upper layers. While the magnitude of $\langle V_z/\overline{N}\rangle^2$ and ε is set primarily by high-frequency waves, the upward energy propagation primarily occurs as near-inertial waves. In this section, we explore whether these empirical relationships are quantitatively supported by existing ideas on the dynamics linking eddies to internal waves. The focus in section 4a is on identifying and quantifying the eddy momentum fluxes that cause a convergence of momentum near the bottom and ultimately lead to the acceleration of deep subinertial velocities. Section 4b tests empirically whether modified linear lee-wave theory can plausibly support the magnitude of turbulent kinetic energy dissipation obtained from the ADCP measurements. Unfortunately, lee-wave crests and troughs are, by definition, stationary with respect to the topography, and are thus not easily observed by a single mooring unless advected either by tides or subinertial flows. Moreover, it is not possible with our mooring observations to quantify the internal wave vertical energy fluxes ($p'w'$) directly as the large gap between the top instruments and the surface (of at least 400 m) leads to large errors in the calculation of vertical modes [Nash et al. (2005) discuss these terms in detail].

a. *Processes controlling acceleration of the lower layers*

In this section, the processes leading to the acceleration of the near-bottom flow at certain points within the time series will be identified. Previous ACC studies (Bryden and Heath 1985; Johnson and Bryden 1989) have invoked quasigeostrophic theory and argued that the net meridional flux $\overline{q'v'}$ of potential vorticity (PV) is balanced by the wind stress τ_x. This PV flux is composed of two components: a meridional divergence of the Reynolds' stress $\rho_0 u'v'$ (termed F_y, where ρ_0 is the background density) and the vertical divergence of the interfacial form stress (termed F_z) (Eliassen and Palm 1961; Edmon et al. 1980):

$$\rho_0\overline{q'v'} = -\frac{\partial}{\partial y}F_y + \frac{\partial}{\partial z}F_z = \frac{\partial \tau_x}{\partial z}. \qquad (6)$$

Primes in the equation represent residuals from the time mean. The quasigeostrophic approximation states that,

for low Rossby number flows, horizontal velocities and advection terms can be replaced by their geostrophic values and that direct vertical advection of momentum (via terms in w) can be neglected.

Unfortunately, the collapse of NE and SW moorings meant that it was impossible to quantify F_y [the first term in Eq. (6)]. While both Johnson and Bryden (1989) and Phillips and Rintoul (2000) have argued that this term is small, this assumption is based on a zonally averaged view of the ACC away from boundaries. Firing et al. (2011) found an along-stream convergence of momentum in the top 1000 m on the southern edge of the SAF and suggested that there may be a divergence on the front's northern flanks. Acknowledging this limitation in our analysis, we nonetheless focus on F_z, which is known to be significant in a region of strongly sloping isopycnals such as the ACC. Here, F_z is defined as follows, where ρ_0 is the background density (1035 kg m^{-3}), σ_θ is the potential density, and the overbar represents the time mean:

$$F_z = \rho_0 f \frac{\overline{\rho' v'}}{\sigma_{\theta_z}}; \tag{7}$$

v is the cross-stream direction at each time step, accounting for orientation changes. The along- and cross-stream directions were defined in shear coordinates between 1234 and 2190 dbar. The F_z estimate was generally insensitive to the choice of these limits. As a comparison with previous studies, the meridional eddy heat flux $\rho_0 c_p \overline{v' T'}$ was also calculated, where c_p is the specific heat at constant pressure (~4000 J kg^{-1} °C^{-1}). Variables T, v, and ρ were bandpass filtered for 40 h–90 days and anomalies were calculated relative to the annual mean at each pressure level.

Profiles of the mean eddy heat flux and interfacial form stress are displayed in Fig. 12. Eddies are responsible for fluxing heat poleward; the largest fluxes occur above 1200 dbar (up to 25 kW m^{-2} at ~500 dbar) but mean values are significantly different from zero at all levels (Fig. 12a). Particularly strong poleward fluxes (exceeding 350 kW m^{-2}) occur as two warm eddies pass immediately to the north of the array on 2 February (Fig. 2e) and 5 September (not shown). Heat fluxes below 1200 dbar are toward the lower end of literature estimates in the region. While DIMES values between 2000 and 3000 dbar are typically 4–5 kW m^{-2} (Fig. 12a), which is comparable to the 4.3 kW m^{-2} observed by Nowlin et al. (1985) at 2660 m in Drake Passage, other estimates tend to be a little higher. For instance, Walkden et al. (2008) estimated a mean heat flux of 12.0 ± 5.8 kW m^{-2} at 2750 m across the Polar Front in Shag Rocks Passage, while Bryden (1979) calculated a flux of

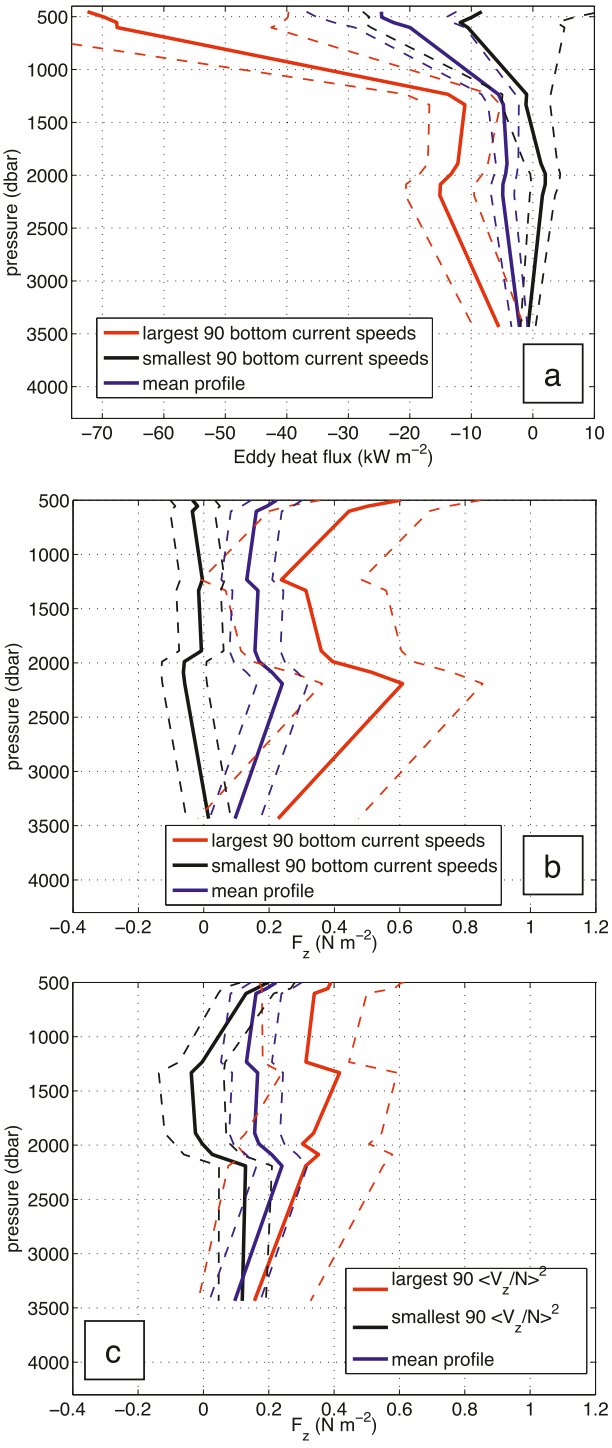

FIG. 12. (a) Mean 359-day cross-stream eddy heat flux at the C mooring (blue), with standard errors in dashed lines. The mean profile for the 90 days with the largest and the smallest bottom current meter speeds are displayed in red and black, respectively, with accompanying standard errors; (b) as Fig. 9a, but for the interfacial form stress F_z; and (c) as Fig. 9b, but for the periods with the highest and lowest normalized shear variance levels $\langle V_z/\overline{N} \rangle^2$, as measured by the Long Ranger ADCP.

6.7 kW m^{-2} at 2700 m. However, it is worth bearing in mind that the value of Bryden did not correct for mooring motion, so it may overestimate by up to 20%.

Owing to the strong poleward heat flux, the mean interfacial form stress is downward, with an average value of 0.17 ± 0.12 N m^{-2} standard error (Fig. 12b). In the mean, the flux is vertically nondivergent, with the reduced poleward heat flux at depth being cancelled out by the weaker stratification. The mean value from this study is in close agreement with values obtained by Johnson and Bryden (1989) and Phillips and Rintoul (2000) and is close to the characteristic value of 0.2 N m^{-2} for the Southern Ocean wind stress.

Also displayed in Fig. 12b are mean F_z profiles for the 90 days on which the near-bottom speed (at 3637 dbar) is highest and the 90 days on which this speed is lowest; F_z is larger at all depths for higher bottom current speeds, but is particularly enhanced around 2000 dbar. While depth-averaged F_z between 1888 and 2190 dbar is 0.47 N m^{-2} for times of elevated current speed, it is −0.04 N m^{-2} when the bottom speed is weak. This results in a strong convergence of F_z between 2190 and 3434 dbar, which acts to accelerate the along-stream near-bottom flow.

As a simple order-of-magnitude estimate of the increase in near-bottom speed caused by this convergence, the mean value of convergence in this layer (3.1×10^{-4} N m^{-3}) is divided by ρ_0 to yield an acceleration. Assuming this acceleration acts upon the water column for 1 day, the change in along-stream velocity is ~0.03 m s^{-1}. This is comparable to the near-bottom speed difference for the 90 highest and lowest profiles (~0.08 m s^{-1}), and thus suggests that convergence of F_z in the bottom kilometer is a significant term in accelerating deep velocities.

The mean F_z profiles for periods with high and low $\langle V_z/\overline{N}\rangle^2$ are shown in Fig. 12c. The vertical structure is similar to Fig. 12b, owing to the positive correlation between near-bottom speed and $\langle V_z/\overline{N}\rangle^2$. However, periods of strong shear variance exhibit a convergence in form stress between ~1200 dbar and the bottom, and the magnitude of the convergence is weaker than in Fig. 12b. This convergence instead yields an increase in speed of 0.012 m s^{-1} day^{-1}. It is likely that this form stress–derived acceleration promotes faster near-bottom speeds, which in turn generates a more vigorous internal wave field through topographic interaction (sections 3d and 4b), leading to stronger TKE dissipation (section 3c).

b. Lee-wave radiation calculation

In light of our observations linking increased geostrophic near-bottom flow to enhanced internal wave activity and stronger dissipation, daily estimates of lee-wave energy radiation from geostrophic flows were calculated based on the methods of Nikurashin and Ferrari (2010a). After least squares fitting of the Goff and Jordan (1988) model to the multibeam bathymetry data, an rms topographic height $h_{\rm rms}$ of 179 m was obtained for the mooring region, with characteristic k_0 and l_0 wavenumbers of the principal axes of topography being 5.1×10^{-4} and 1.9×10^{-4} m^{-1}, respectively. The topographic hill is thus anisotropic, with the principal axis being oriented at 136°/316° (Fig. 13a). Daily estimates of bottom current speed and direction were obtained from the 40-h low-pass-filtered bottom current meter time series, and N^2 values were calculated from the bottom two MicroCAT instruments. Time series of lee-wave energy radiation $E_{\rm rad}$ were then calculated according to

$$E_{\rm rad} = \frac{\rho_0 |\mathbf{U}_0|}{2\pi} \int_{f/|U_0|}^{N/|U_0|} dk \sqrt{(|\mathbf{U}_0|^2 k^2) - f^2} \sqrt{N^2 - (|\mathbf{U}_0|^2 k^2)} \; \frac{1}{2\pi} \int_{-\infty}^{+\infty} \frac{|k|}{|\mathbf{k}|} P(\mathbf{k})\, dl, \tag{8}$$

where $\mathbf{U}_0$ is the low-pass-filtered current velocity, $\mathbf{k} = (k, l)$ is the horizontal wavenumber vector along and across the mean flow, and $P(\mathbf{k})$ is the 2D topography spectrum. To account for saturation of the energy flux that occurs at supercritical topography, the steepness parameter $L = N\sqrt{2h}/U_0$ is calculated, where h is the topographic height in the radiative wavenumber range. When this value exceeds 0.7, $E_{\rm rad}$ is multiplied by $(0.7/L)^2$.

Three time series of radiation were calculated, one using the actual current speed and direction on each day, the other two orienting the flow on each day directly along and directly across the topography to yield the maximum and minimum theoretical radiation for that speed independent of its direction. These time series are displayed in Fig. 13b.

The annual-mean energy radiation predicted for the region is 5.3 mW m^{-2}, with a maximum value of 185 mW m^{-2} on 4 February and a strongly asymmetric distribution (over 200 daily values are less than 1 mW m^{-2}). The mean value is similar to the section-averaged western Drake Passage value (3.1 mW m^{-2}) in western Drake Passage, computed using 1D spectra by Sheen et al. (2013). The mean steepness parameter, which in part determines the ability of lee waves to propagate from the bottom, is 0.71 ± 0.08 (Fig. 13d), a value close to the critical figure of 0.7 at which energy conversion saturates. As expected,

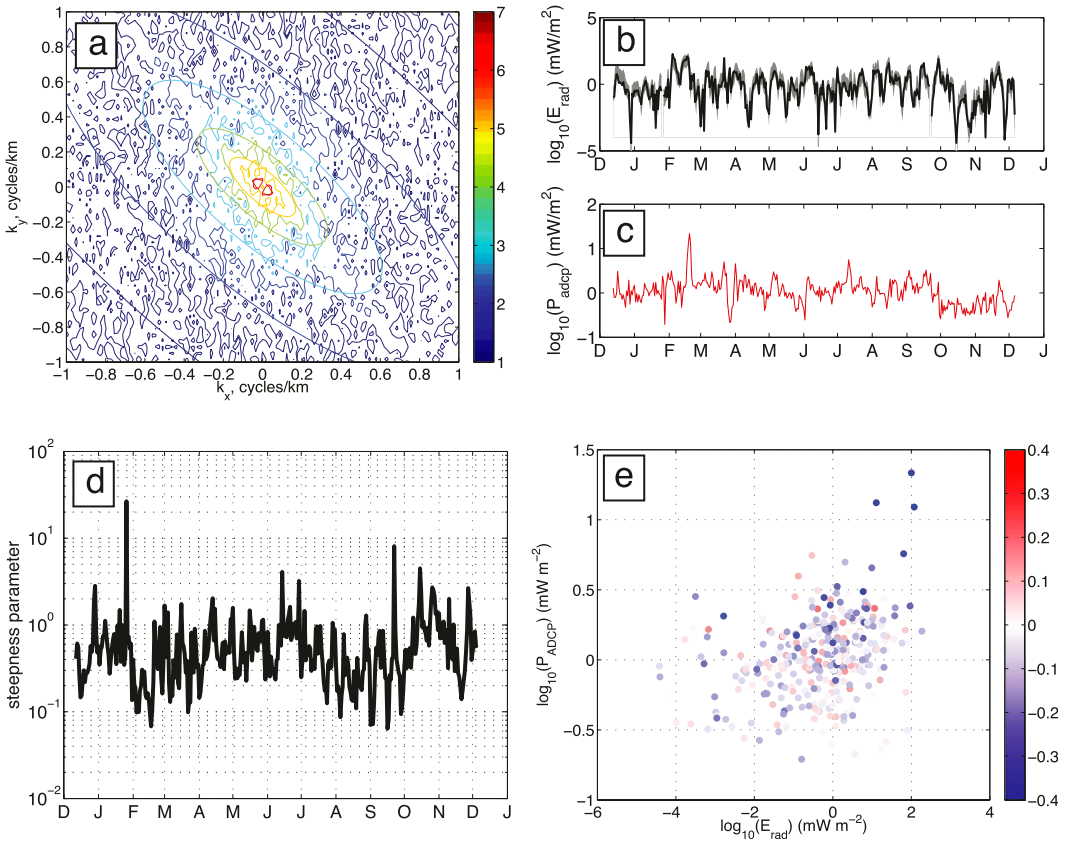

FIG. 13. (a) 2D topography power spectrum $\{\log_{10}[\mathbf{P}(k_x, k_y)]\}$ of the mooring region(m^2 km^2 cycle^{-2}), with the best fit Goff and Jordan (1988) model contoured. The roll-off parameter is set to 4. (b) Time series of lee-wave radiation E_{rad} predicted from linear theory. The edges of the shaded region indicate max and min possible radiation assuming the most and least preferential current orientations at each time step. (c) Time series of dissipated power in the bottom 900 m inferred from the time series of ADCP ε; (d) time series of steepness parameter L; and (e) scatterplot of daily values of dissipated power against E_{rad}, color coded by rotary coefficient [$\log_{10}$(CCW/CW)].

E_{rad} exhibits a strong positive correlation with U_0 ($r = 0.73$, $p < 0.01$, and df = 157). The minimum and maximum radiation curves, shown as the upper and lower limits in Fig. 13b, have mean values of 1 and 11 mW m^{-2}, respectively.

To assess whether enough energy is generated by lee waves to account for the magnitude of dissipation observed by the ADCP, the fine structure–based daily estimates of dissipation between ~2800 and ~3300 m were extrapolated over the bottom 900 m to give an estimate of total power dissipated between the ADCP transducer and the ocean floor. The two time series are plotted above one another in Figs. 13b,c. The ratio of dissipated to radiated power ($E_{\text{diss}}/E_{\text{rad}}$) was also calculated.

Over the year as a whole, and based on mean radiated power and mean dissipation, ~21% of E_{rad} is dissipated in the bottom 900 m, assuming that the dissipation inferred from the ADCP is also representative of dissipation values in the region between 3300 m and the bottom. This would suggest that existing lee-wave theory can plausibly sustain the TKE dissipation estimated from observations. However, there is clearly a discrepancy in the size of the values.

If median (instead of mean) values of radiated and dissipated power are used instead, a much closer agreement is found (the values are 0.86 and 0.71 mW m^{-2}). The difference between the two measures of central tendency is explained by the large positive skewness to the radiation distribution (there are a few E_{rad} values of over 100 mW m^{-2} that cannot be dissipated near the bottom). Furthermore, the day-to-day variability of E_{rad} (as measured by the standard deviation of the time series) is much larger than for E_{diss} (17.0 mW m^{-2} compared with 1.6 mW m^{-2}).

Linear theory also provides an estimate for the wavelengths of the radiated lee waves. This is given by $\lambda = 2\pi U_0/N_0$ (Gill 1982), and the annual-mean (median) wavelength is 512 m (381 m). Predicted wavelengths increase rapidly with U_0, such that bottom speeds exceeding 10 cm s^{-1} have typical wavelengths of 1–3 km.

Periods of high near-bottom current speed (and long wavelengths) tend to coincide with the largest difference between E_{rad} and E_{diss}. In any case, the predicted wavelengths of lee waves are much longer than the integration limits of the finescale parameterization (130–320 m), implying that lee-wave energy must be transferred to higher-frequency (and shorter wavelength) internal waves that provide the majority of the observed shear variance (section 3). Furthermore, the wavelengths predicted by linear theory may be in error, in part due to the assumption of steady flow, or alternatively the disregard of finite-amplitude topographic effects (Sheen et al. 2013). Moreover, some of this internal wave energy may be dissipated nonlocally, which may explain part of the mismatch between E_{rad} and E_{diss}, though the large L would suggest that lee-wave energy cannot propagate too far.

While the mean dissipation values observed here appear to be insufficient to remove the energy radiated from the sea floor as lee waves, elevated values of E_{diss} do generally coincide with high E_{rad} (Fig. 13e). Furthermore, periods of particularly high radiation/dissipation show a tendency to be associated with a negative rotary coefficient, though we acknowledge that this relationship is dominated by a relatively small number of data points. The correlation for the year as a whole between E_{diss} and E_{rad} is 0.41 ($p < 0.01$, df = 212), but increases to 0.71 ($p < 0.01$, df = 29) for the 50 days on which the rotary coefficient is smallest (i.e., there is a predominance of upward-propagating energy). However, the first linear regression coefficient (which determines the slope) is small; for each 100 mW m^{-2} increase in E_{rad}, E_{diss} only increases by 3.8 mW m^{-2}. As already discussed, this may be attributable either to errors in the lee-wave prediction or by dissipation of energy further away from the topography.

There is no clear evidence in this dataset for the directionality of near-bottom flow affecting the magnitude of E_{diss}. While the correlation between E_{rad} (using the real current directions) and E_{diss} was 0.41, the correlation is actually larger if the maximum or minimum radiation time series are used instead of E_{rad} ($r = 0.46$) (Fig. 13b). This is surprising given the anisotropy of the topography (Fig. 13a), but further analysis confirmed that there was no preferential directional enhancement of $\langle V_z/\overline{N}\rangle^2$. One possible explanation is that the topographic obstacle does not exist in isolation; in reality the western Scotia Sea is characterized by large numbers of abyssal hills with enhanced h_{rms}. Indeed, the multibeam data (Fig. 1b) suggest that there may be similar hills a few kilometers to both the northwest and southeast of the moorings. Whether the shear variance dissipated at the C mooring is solely generated at the bump or is sourced from a wider region is not clear.

In summary, the energy flux predicted by modified linear lee-wave theory is sufficient to support the integrated dissipation in the bottom 900 m. Furthermore, a modest but significant correlation is observed between the E_{rad} and E_{diss} inferred from the finescale parameterization. The discrepancy between E_{diss} and E_{rad}, which is accentuated when the predicted radiation is large, is probably accounted for in part by assumptions in linear lee-wave theory and possibly also by more distant dissipation. A final observation is that much of the energy radiated (and dissipated) occurs in a number of isolated events (e.g., the 10 days with the largest dissipated power make up 16% of the total annual dissipation). This highlights the limitations in estimating time- and space-averaged values of internal wave energy and ε from individual microstructure or ADCP sections.

5. Conclusions

This study has presented a year of hydrographic and velocity data from a cluster of moorings located over a ~700-m-tall topographic obstacle in the ACC to the east of Drake Passage. Dissipation has been inferred based on a fine-structure parameterization to assess mixing due to internal wave breaking. Using these measurements, we have argued that a significant transfer of energy occurs between mesoscale eddies, internal waves, and turbulent dissipation.

Periods of enhanced shear variance at hundred-meter scales (and dissipation) coincide with an increase in upward-propagating bottom-sourced internal wave energy and an intensification of subinertial near-bottom current speed ($r = 0.45$). Although some enhanced variability of shear variance at tidal frequencies was also observed, there is no obvious modulation of $\langle V_z/\overline{N}\rangle^2$ at spring–neap time scales (14 days) and the barotropic tides themselves are relatively weak (0.7–1.3 cm s^{-1}), suggesting that conversion of barotropic tidal energy into $O(100\,\text{m})$ shear is likely to be a second-order effect.

It is argued that this intensification in near-bottom speed is driven at least in part by an overall increase of (and convergence in) interfacial form stress in the lower part of the water column (F_z). The magnitude of F_z changes appears to be sufficiently large to account for much of the observed acceleration of the near-bottom flow, though we do not discount the possibility that Reynolds' stress convergence also plays a role. The bottom-flow acceleration in turn promotes the generation and radiation of lee waves. The size of this radiation flux (predicted from modified linear lee-wave theory) is more than sufficient to support the observed dissipation levels in the bottom 900 m of the water column.

The results pose a number of challenges. First, obtaining stable estimates of the vertical internal wave energy flux from moorings sampling at discrete depths (such as those in this study) remains a key priority, as convergence of these fluxes would provide empirical evidence of the internal wave breaking that ultimately leads to dissipation. Second, identifying the dynamics linking near-inertial waves (which show the strongest polarization) and high-frequency waves (which account for the bulk of the shear variance) is key to understanding the final steps in the downscale cascade of energy that results in turbulent dissipation. Finally, the lack of correlation between integrated shear variance and flow directionality, despite the anisotropic topography, poses questions as to the length scales over which two-dimensional topography spectra have to be evaluated when estimating lee-wave radiation, especially in regions of complex topography.

It is germane to consider how applicable the processes we have identified are to the entire Southern Ocean. The study has provided evidence supporting an eddy-internal wave energy transfer in a region where lee-wave theory contends that the process should operate. However, the rms height of the topography (179 m) here is not atypical; indeed the value exceeds 300 m in much of Drake Passage (Sheen et al. 2013). Furthermore, the magnitude of eddy flows is not exceptional (Morrow et al. 1994) compared with other regions of the Southern Ocean (e.g., the Indian Ocean sector). It can, therefore, be assumed that this process operates in much of the Southern Ocean where rough topography is present, and thus forms a globally significant sink of EKE (Nikurashin and Ferrari 2011; Scott et al. 2011).

As outlined earlier, several model and observational studies have predicted an increase in Southern Ocean wind stress in coming decades. Much of this energy will be transferred into the eddy field (Allison et al. 2010; Abernathey et al. 2011), and it is tempting to speculate on the consequences for the internal wave field, via the mechanism identified in this study. Answering these questions will be key to understanding the impact of eddies on mixing and their role in the Southern Ocean limb of the Meridional Overturning Circulation.

Acknowledgments. We thank Dr. Nathan Cunningham at Schmidt Ocean (formerly at BAS) for processing the multibeam data and Dr. Xinfeng Liang at LDEO for assistance with the wavelet analysis. Comments on the manuscript by Dr. Kurt Polzin at WHOI and three anonymous reviewers are gratefully acknowledged. Funding for the U.K. component of DIMES was provided by the Natural Environment Research Council, Grant NE/F020252/1. We thank the technicians and crew of RRS *James Cook*.

REFERENCES

Abernathey, R., J. Marshall, and D. Ferreira, 2011: The dependence of Southern Ocean meridional overturning on wind stress. *J. Phys. Oceanogr.,* **41,** 2261–2278.

Allison, L. C., H. L. Johnson, D. P. Marshall, and D. R. Munday, 2010: Where do winds drive the Antarctic Circumpolar Current? *Geophys. Res. Lett.,* **37,** L12605, doi:10.1029/2010GL043355.

Bell, T. H., Jr., 1975: Topographically generated internal waves in the open ocean. *J. Geophys. Res.,* **80,** 320–327.

Bryden, H. L., 1979: Poleward heat flux and conversion of available potential energy in Drake Passage. *J. Mar. Res.,* **37,** 1–22.

——, and R. A. Heath, 1985: Energetic eddies at the northern edge of the Antarctic Circumpolar Current. *Prog. Oceanogr.,* **14,** 65–87.

Chereskin, T. K., K. A. Donohue, D. R. Watts, K. L. Tracey, Y. L. Firing, and A. L. Cutting, 2009: Strong bottom currents and cyclogenesis in Drake Passage. *Geophys. Res. Lett.,* **36,** L23602, doi:10.1029/2009GL040940.

Collins, J. J., J. Molina, T. Kanzow, S. Cunningham, and W. Johns, 2008: Processing and management of the RAPID-MOC/MOCHA mooring array data. National Oceanography Centre Internal Rep., 39 pp.

Cronin, M., K. L. Tracey, and D. R. Watts, 1992: Mooring motion correction of the SYNOP central array current meter data. GSO Tech. Rep. 92–4, 114 pp.

Damerell, G. M., K. J. Heywood, D. P. Stevens, and A. C. Naveira Garabato, 2011: Temporal variability of diapycnal mixing in Shag Rocks Passage. *J. Phys. Oceanogr.,* **42,** 370–385.

Edmon, H. J., B. J. Hoskins, and M. E. McIntyre, 1980: Eliassen–Palm cross sections for the troposphere. *J. Atmos. Sci.,* **37,** 2600–2616.

Eliassen, A., and E. Palm, 1961: On the transfer of energy in stationary mountain waves. *Geofys. Publ.,* **22,** 1–23.

Ferrari, R., and C. Wunsch, 2009: Ocean circulation kinetic energy: Reservoirs, sources, and sinks. *Annu. Rev. Fluid Mech.,* **41,** 253–282.

Firing, Y. L., T. K. Chereskin, and M. R. Matzloff, 2011: Vertical structure and transport of the Antarctic Circumpolar Current in Drake Passage from direct velocity observations. *J. Geophys. Res.,* **116,** C08015, doi:10.1029/2011JC006999.

Garrett, C., and W. Munk, 1975: Space-time scales of internal waves—Progress report. *J. Geophys. Res.,* **80,** 291–297.

——, and ——, 1976: Internal waves in the ocean. *Annu. Rev. Fluid Mech.,* **11,** 339–369.

Gill, A. E., 1982: *Atmosphere–Ocean Dynamics.* Academic Press, 662 pp.

Gille, S. T., 1994: Mean sea surface height of the Antarctic circumpolar current from GEOSAT data: Methods and application. *J. Geophys. Res.,* **99** (C9), 18 255–18 273.

Goff, J. A., and T. H. Jordan, 1988: Stochastic modeling of seafloor morphology: Inversion of sea beam data for second order statistics. *J. Geophys. Res.,* **93,** 13 589–13 608.

Gregg, M. C., T. B. Sanford, and D. P. Winkel, 2003: Reduced mixing from the breaking of internal waves in equatorial waters. *Nature,* **422,** 513–515.

Henyey, F. S., J. Wright, and S. M. Flatté, 1986: Energy and action flow through the internal wave field: An eikonal approach. *J. Geophys. Res.,* **91** (C7), 8487–8495.

Hogg, N. G., 1986: On the correction of temperature and velocity time series for mooring motion. *J. Atmos. Oceanic Technol.,* **3,** 204–214.

——, 1991: Mooring motion corrections revisited. *J. Atmos. Oceanic Technol.,* **8,** 289–295.

Johnson, G. C., and H. L. Bryden, 1989: On the size of the Antarctic Circumpolar Current. *Deep-Sea Res.,* **36,** 35–53.

Klymak, J. M., R. Pinkel, and L. Rainville, 2008: Direct breaking of the internal tide near topography: Kaena Ridge, Hawaii. *J. Phys. Oceanogr.,* **38,** 380–399.

Kunze, E., L. K. Rosenfeld, G. S. Carter, and M. C. Gregg, 2002: Internal waves in Monterey Canyon. *J. Phys. Oceanogr.,* **32,** 1890–1913.

——, E. Firing, J. M. Hummon, T. K. Chereskin, and A. M. Thurnherr, 2006: Global abyssal mixing inferred from lowered ADCP shear and CTD strain profiles. *J. Phys. Oceanogr.,* **36,** 1553–1576.

Ledwell, J. R., L. C. St. Laurent, J. B. Girton, and J. M. Toole, 2011: Diapycnal mixing in the Antarctic Circumpolar Current. *J. Phys. Oceanogr.,* **41,** 241–246.

Liang, X., and A. M. Thurnherr, 2012: Eddy-modulated internal waves and mixing on a midocean ridge. *J. Phys. Oceanogr.,* **42,** 1242–1248.

Maximenko, N., P. Niiler, L. Centurioni, M.-H. Rio, and O. Melnichenko, 2009: Mean dynamic topography of the ocean from satellite and drifting buoy data using three different techniques. *J. Atmos. Oceanic Technol.,* **26,** 1910–1919.

Meredith, M. P., 2011: Cruise report: RRS *James Cook* JC054 (DIMES UK2) 30 Nov 2010 to 8 Jan 2011. British Antarctic Survey Cruise Rep., 206 pp.

——, and A. M. Hogg, 2006: Circumpolar response of Southern Ocean eddy activity to a change in the southern annular mode. *Geophys. Res. Lett.,* **33,** L16608, doi:10.1029/2006GL026499.

——, A. C. Naveira Garabato, A. M. Hogg, and R. Farneti, 2012: Sensitivity of the overturning circulation in the Southern Ocean to decadal changes in wind forcing. *J. Climate,* **25,** 99–110.

Molemaker, M. J., J. C. McWilliams, and X. Capet, 2010: Balanced and unbalanced routes to dissipation in an equilibrated Eady flow. *J. Fluid Mech.,* **654,** 35–63.

Morrow, R. A., R. Coleman, J. A. Church, and D. B. Chelton, 1994: Surface eddy momentum flux and velocity variances in the Southern Ocean from *Geosat* altimetry. *J. Phys. Oceanogr.,* **24,** 2050–2071.

Nash, J. D., M. H. Alford, and E. Kunze, 2005: Estimating internal wave energy fluxes in the ocean. *J. Phys. Oceanogr.,* **22,** 1552–1570.

Naveira Garabato, A. C., K. L. Polzin, B. A. King, K. J. Heywood, and M. Visbeck, 2004: Widespread intense turbulent mixing in the Southern Ocean. *Science,* **303,** 210–213.

Nikurashin, M., and R. Ferrari, 2010a: Radiation and dissipation of internal waves generated by geostrophic flows impinging on small-scale topography: Theory. *J. Phys. Oceanogr.,* **40,** 1055–1074.

——, and ——, 2010b: Radiation and dissipation of internal waves generated by geostrophic motions impinging on small-scale topography: Application to the Southern Ocean. *J. Phys. Oceanogr.,* **40,** 2025–2042.

——, and ——, 2011: Global energy conversion rate from geostrophic flows into internal lee waves in the deep ocean. *Geophys. Res. Lett.,* **38,** L08610, doi:10.1029/2011GL046576.

Nowlin, W. D., Jr., S. J. Worley, and T. Whitworth III, 1985: Methods for making point estimates of eddy heat flux as applied to the Antarctic Circumpolar Current. *J. Geophys. Res.,* **90** (C2), 3305–3324.

Orsi, A. H., T. Whitworth III, D. Worth, and W. D. Nowlin Jr., 1995: On the meridional extent and fronts of the Antarctic Circumpolar Current. *Deep-Sea Res. I,* **42,** 641–673.

Pawlowicz, R., B. Beardsley, and S. Lentz, 2002: Classical tidal harmonic analysis including error estimates in MATLAB using T_TIDE. *Comput. Geosci.,* **28,** 929–937.

Phillips, H. E., and S. R. Rintoul, 2000: Eddy variability and energetics from direct current measurements in the Antarctic Circumpolar Current south of Australia. *J. Phys. Oceanogr.,* **30,** 3050–3076.

Polzin, K., J. M. Toole, and R. W. Schmitt, 1995: Finescale parameterizations of turbulent dissipation. *J. Phys. Oceanogr.,* **25,** 306–328.

——, ——, J. R. Ledwell, and R. W. Schmitt, 1997: Spatial variability of turbulent mixing in the abyssal ocean. *Science,* **276** (5309), 93–96, doi:10.1126/science.276.5309.93.

——, E. Kunze, J. Hummon, and E. Firing, 2002: The finescale response of lowered ADCP velocity profiles. *J. Phys. Oceanogr.,* **19,** 205–224.

Scott, R. B., and F. M. Wang, 2005: Direct evidence of an oceanic inverse kinetic energy cascade from satellite altimetry. *J. Phys. Oceanogr.,* **35,** 1650–1666.

——, J. A. Goff, A. C. Naveira Garabato, and A. J. G. Nurser, 2011: Global rate and spectral characteristics of internal gravity wave generation by geostrophic flow over topography. *J. Geophys. Res.,* **116,** C09029, doi:10.1029/2011JC007005.

Sheen, K. L., and Coauthors, 2013: Rates and mechanisms of turbulent dissipation and mixing in the Southern Ocean: Results from the DIMES experiment. *J. Geophys. Res.,* **118,** 2774–2792, doi:10.1002/jgrc.20217.

Smith, K. S., 2007: The geography of linear baroclinic instability in Earth's oceans. *J. Mar. Res.,* **29,** 655–683.

St. Laurent, L., A. C. Naveira Garabato, J. R. Ledwell, A. M. Thurnherr, J. M. Toole, and A. J. Watson, 2012: Turbulence and diapycnal mixing in Drake Passage. *J. Phys. Oceanogr.,* **42,** 2143–2152.

Thompson, D. W. J., and S. Solomon, 2002: Interpretation of recent Southern Hemisphere climate change. *Science,* **296,** 895–899.

Walkden, G. J., K. J. Heywood, and D. P. Stevens, 2008: Eddy heat fluxes from direct current measurements of the Antarctic Polar Front in Shag Rocks Passage. *Geophys. Res. Lett.,* **35,** L06602, doi:10.1029/2007GL032767.

Waterman, S., K. L. Polzin, and A. C. Naveira Garabato, 2013a: Internal waves and turbulence in the Antarctic Circumpolar Current. *J. Phys. Oceanogr.,* **43,** 259–282.

Wunsch, C., and D. Stammer, 1998: Satellite altimetry, the marine geoid and the oceanic general circulation. *Annu. Rev. Earth Planet. Sci.,* **26,** 219–254.

——, and R. Ferrari, 2004: Vertical mixing, energy and the general circulation of the oceans. *Annu. Rev. Fluid Mech.,* **36,** 281–314.

Zaron, E. D., C. Chavanne, G. D. Egbert, and P. Flament, 2009: Baroclinic tidal generation in the Kauai Channel inferred from high-frequency radio Doppler current meters. *Dyn. Atmos. Oceans,* **48,** 93–120.